Title: Mapping spatially-resolved transcriptomes in systemic sclerosis

Authors: Zhijian Li[1,2], Aleix Rius Rigau[3,4], Wenjie Xie[5], Linlin Huang[6,7,8], Xiaohang Shao[9], Yi-Nan Li[10,11], Alexandru-Emil Matei[10,11], Wenjing Ye[6,7,8], Hejian Zou[6,7,8], Luca Pinello[1,2,12], Jörg H.W. Distler[10,11*], Rui He[5,13*], and Minrui Liang[6,7,8*]

Affiliations:

[1]Broad Institute of Harvard and MIT, Cambridge, MA, USA.

[2]Molecular Pathology Unit, Center for Cancer Research, Massachusetts General Hospital, Boston, MA, USA.

[3]Department of Internal Medicine 3, Rheumatology and Clinical Immunology, Friedrich-Alexander-University Erlangen-Nürnberg (FAU) and University Hospital Erlangen, Erlangen, Germany.

[4]Deutsches Zentrum Immuntherapie (DZI), FAU Erlangen-Nürnberg and University Hospital Erlangen, Erlangen, Germany.

[5]Department of Immunology, School of Basic Medical Sciences, Fudan University, Shanghai, China.

[6]Department of Rheumatology, Huashan Hospital, Fudan University, Shanghai, China.

[7]Institute of Rheumatology, Immunology and Allergy, Fudan University, Shanghai, China.

[8]Huashan Rare Disease Center, Huashan Hospital, Fudan University, Shanghai, China.

[9]Department of Nephrology and Rheumatology Immunology, Ningbo Medical Center Lihuili Hospital, Ningbo, China.

[10]Clinic for Rheumatology, University Hospital Düsseldorf, Medical Faculty of Heinrich Heine University, Düsseldorf, Germany.

[11]Hiller Research Center, University Hospital Düsseldorf, Medical Faculty of Heinrich Heine University, Düsseldorf, Germany.

[12]Department of Pathology, Harvard Medical School, Boston, MA, USA.

[13]National Clinical Research Center for Aging and Medicine, Huashan Hospital, Fudan University, Shanghai, 200040, China.

* Correspondence to Prof. Minrui Liang: mliang10@fudan.edu.cn; Prof. Rui He: ruihe@fudan.edu.cn; Univ. Prof. Dr. med. Jörg H.W. Distler: Joerg.Distler@med.uni-duesseldorf.de;

Abstract: Systemic sclerosis (SSc) is a prototypical fibrotic disease with high mortality and limited treatment options. Despite advances in single-cell RNA sequencing (scRNA-seq), the comprehensive understanding of cellular heterogeneity and cell-cell interaction within the fibrogenesis microenvironment remains limited. We generated spatially resolved transcriptome maps from healthy and SSc skin and built a scRNA-seq atlas to map the single-cell data to spatial space. This enabled us to identify a fibrotic niche, enriched with fibroblasts and macrophages, which is significantly expanded in SSc and correlated with clinical outcome. We revealed disease-specific cell states of fibroblasts and macrophages, and evaluated their spatial dependency on other cell types. We identified selective expression of ACKR3 in fibroblast progenitors that diminishes with SSc progression, which may serve to regulate CXCL12/CXCR4-mediated macrophage recruitment and fibrotic remodeling. Together, we provided an in-depth description at cellular and spatial levels of fine-tuned regulatory events occurring in SSc, offering spatiotemporal insights.

One Sentence Summary:

Integrated spatial omics provide insight into the cellular and transcriptional landscape in spatially distinct microenvironments, which may drive fibrosis progression in SSc.

Main Text:

INTRODUCTION

Systemic Sclerosis (SSc), an orphan autoimmune disease, is characterized by the progressive fibrosis affecting skin and multiple organs, holding the highest mortality among all rheumatic diseases(*1*). The development of effective therapeutic strategies for SSc is impeded by a lack of comprehensive understanding of its pathogenesis and the limited translatability of current preclinical models. Importantly, studying SSc as a prototypical systemic fibrotic disease could yield new insights into the pathogenesis of fibrotic diseases, and aid in the discovery of novel therapeutic approaches.

SSc is characterized by a complex interplay of features that include vasculopathy, inflammation, and fibrosis. Within this triad, fibroblasts have been recognized as pivotal effector cells in the production of extracellular matrix (ECM), largely contributing to developing fibrotic tissue remodeling in SSc. Fibroblasts sense and receive signaling from the neighboring cells, which are conveyed and converge to the shared and distinct profibrotic pathways(*2*). The coordination of fibroblasts with macrophages can shape their cellular response, therefore orchestrating the initiation or resolution of fibrosis across tissues(*3–7*). Beyond the conventional macrophage polarization paradigm, new populations of macrophages have been linked with tissue repair and fibrotic remodeling(*3–5*, *7*, *8*). For instance, phenotypically distinct macrophages (Lyve1^{lo}MHCII^{hi} and Lyve1^{hi}MHCII^{lo}) manifested specific niche-dependent functional roles in pulmonary and cardiac fibrosis(*8*). However, it remains largely unexplored whether and how the spatial neighbourhood in the tissue architecture affects the crosstalk between fibroblast and macrophage subsets, potentially driving fibrotic remodeling in SSc.

Recent studies using single-cell RNA sequencing (scRNA-seq) have provided an unprecedented opportunity to study the molecular mechanisms of SSc at single-cell resolution(*9–13*). Pioneering studies have characterized fibroblast types and states in SSc(*9*, *11*, *13*). While these studies have provided valuable insights, they are significantly constrained by the lack of spatial resolution due to the reliance on disaggregated tissue analysis. We recently demonstrated cellular niches centered around endothelial cells or fibroblasts in SSc using a panel of up to 40 markers through multiplex spatial proteomics(*14*, *15*). Thus, a spatially-resolved characterization of genome-wide transcriptomics of SSc is needed.

In this work, we profiled human skin from SSc patients and healthy controls using spatial transcriptomics (ST) technique based on the 10x Visium formalin-fixed paraffin-embedded (FFPE) platform and spatial enhanced resolution omics sequencing (Stereo-seq)(*16*). To increase the cellular resolution of our ST data, we integrated two publicly available scRNA-seq datasets, creating a human skin transcriptome atlas and mapping cell type information onto spatial regions. We validated our results using additional spatial profiling techniques with higher resolution, such as imaging mass cytometry (IMC), as well as time-course experimental skin fibrosis. These approaches enabled us to reveal a detailed characterization of pathological cellular communication between fibroblast and macrophage subsets. This has provided insights into therapeutic target discovery by disrupting disease-driving cellular niches and circuits in SSc.

RESULTS

Profiling of SSc and healthy skin with spatially-resolved transcriptomics

We collected a total of 14 human skin biopsies from 10 SSc patients enriched for early-stage, diffuse cutaneous involvement, with clinically active disease and 4 sex- and age- matched normal controls (**Fig. 1A and table S1**). For each biopsy, we generated spatially resolved transcriptomics (ST) using the 10x Visium platform. After removing low-quality spots across all samples, we retained 13,204 high quality spots with a median detection of 2,265 genes per spot (**figs. S1, A to D, and table S2**). To enhance spatial resolution, we also performed high-resolution ST profiles on four samples, one from a healthy donor and three from SSc patients, using Stereo-seq. After controlling data quality, we retained 40,566 spots across these samples. We additionally analyzed two scRNA-seq datasets generated from skin tissues of SSc patients (n = 104) and healthy donors (n = 64)(*9*, *10*). The cells were re-annotated for each dataset based on clustering or the original labels (**figs. S2, A to D; see Materials and Methods**). We integrated the scRNA-seq datasets and observed that the same cell types were well-aligned in the UMAP space, which was further confirmed by the cell-type-specific marker genes identified based on the integrated profiles (**Figs. 1, B to C, figs. S2, E to G**). Together, these data provide a comprehensive multi-modal map of human skin tissues in health and SSc, capturing both spatial and single-cell transcriptomic landscapes.

We next deconvoluted the cell-type compositions of each spot in 10x Visium data using the

125 scRNA-seq as reference. The estimated cell type abundances from spatial transcriptomics were
126 generally co-localized with their respective marker genes (**Fig. 1D**). Moreover, we observed
127 that different cell types were mapped to the expected locations. For example, keratinocytes
128 were found localized within the epidermis and surrounding the hair follicle. Endothelial cells
129 were closely associated with vasculature in the dermis. Fibroblasts were distributed throughout
130 the papillary layer and reticular layer of the dermis. We inferred the pathway activity for each
131 spot and observed the enriched expression of genes associated with some well-known pathways,
132 such as Janus kinase signal transducer and activator of transcription protein (JAK-STAT) and
133 transforming growth factor (TGF)-β, reflecting the link between cellular location and the
134 corresponding function (**Fig. 1D**). We transferred the cell type annotation from scRNA-seq to
135 Stereo-seq through data integration (**Fig. 1E**). Spatial visualization of the predicted labels in
136 tissues showed a similar cellular distribution as 10x Visium data (**Fig. 1F**). Collectively, our
137 integrative analyses on spatial transcriptomics and scRNA-seq data enable us to map cell
138 abundance and signaling pathways across zonations in skin samples.
139
140 **Characterization of tissue organization in SSc and healthy skin**
141 To characterize the cellular colocalization events in human skin, we integrated the 10x Visium
142 samples (n = 14) based on the inferred cell-type proportions within each spot (**fig. S3A**).
143 Specifically, we conducted spot deconvolution to determine the proportions of different cell
144 types within each spot, and subsequently clustered the spots based on these identified
145 proportions (**Fig. 2A**). Clustering analysis identified 12 compositionally distinct populations,
146 defined as cell-type niches that represent potential structural building blocks shared across
147 different samples. Visualization of the cell-type abundances and marker genes of these niches
148 revealed that they were strongly associated with the corresponding cell types (**Fig. 2B, figs. S3,**
149 **B to C**). For example, niches 1 and 3 (defined as vasculature niches) were enriched with
150 endothelial cells and pericytes; niches 0 and 10 (defined as fibrotic niches) were enriched with
151 fibroblasts; niches 6, 7 and 8 (defined as epidermis niches) were largely associated with
152 keratinocyte as the representative cell types and along with the infiltration of Langerhans cells;
153 niche 11 was related to vascular smooth muscle cells (VSMC) and therefore defined as a
154 VSMC niche; niche 2, 4, 5, and 9 (defined as immune niches) were related to immune cells
155 (**Fig. 2C**).
156
157 Furthermore, we observed a significant increase in the proportions of three niches (0, 1, and 4)
158 in the SSc skin compared to healthy skin (**Figs. 2, D to E, fig. S3D**). Notably, niche 0 was

159 infiltrated with a high prevalence of fibroblasts, macrophages, conventional dendritic cells
160 (cDCs), and mast cells, indicating a potential immune microenvironment within a fibrogenic
161 niche. Niche 1 was characterized by an enrichment of endothelial cells, pericytes, macrophages,
162 cDCs, and mast cells, suggesting a perivascular niche associated with immune cell infiltration
163 in SSc skin. Additionally, niche 4 was distinguished by a significant presence of plasma cells,
164 melanocytes, and neural cells (**Fig. 2C**). Moreover, SSc skin exhibited a more reorganized
165 structure, highlighting a tendency towards spatially educated organization, with a dominance
166 in niche distribution (**Fig. 2E, fig. S3D**).
167
168 To investigate the featured signaling pathway that characterizes each specific niche, we
169 computed pathway activity. Fibroblast-dominant niche 0 showed the highest activity of the
170 TGF-β signaling pathway. Niche 9, composed of various immune cells, displayed the strongest
171 activity of JAK-STAT signaling (**Fig. 2F**). These findings supported the essential roles of TGF-
172 β and JAK-STAT signaling in the pathogenesis of SSc as expected(*2*), suggesting a
173 convergence of multiple signaling activities within the structural organization in SSc fibrosis.
174 KEGG pathway enrichment analysis based on marker genes also revealed high activity in the
175 TGF-β signaling in niche 0 (**fig. S3E**).
176
177 Indeed, we observed colocalization of fibroblasts and macrophages in our 10x Visium and
178 Stereo-seq data (**Figs. 2, G to H**). To further validate these results, we performed imaging mass
179 cytometry (IMC) and identified the cellular neighborhood (CN) community as described
180 previously(*14*). We observed similar niches comprising stromal cells and macrophages (CN8),
181 vascular ECs, and immune cells, including macrophages in CN5 (**figs. S4, A to C**). To explore
182 the clinical relevance of these niches, we correlated their proportions with clinical data across
183 the SSc samples. Interestingly, we observed a positive Spearman correlation between the
184 proportion of niche 0 and the current total modified Rodnan's skin score (mRSS) ($r = 0.733$, p
185 $= 0.023$), C-reactive protein (CRP) levels ($r = 0.750$, $p = 0.066$) and platelet counts ($r = 0.697$,
186 $p = 0.031$), which are interpreted as clinical indicators for disease severity or activity of SSc
187 (**Fig. 2I**). Additionally, we observed a significant inverse correlation between the proportion
188 of niche 1 and the non-Raynaud's phenomenon (RP) disease duration ($r = -0.756$, $p = 0.014$).
189 In summary, our spatial multi-omics revealed a distinct structural organization associated with
190 disease outcome of SSc, suggesting a potential coordinated regulation of immune-stromal
191 interactions that may drive the disease progression.
192

193 **Characterization of fibroblast sub-clusters in healthy and SSc skin**

194 To investigate the molecular mechanisms driving fibrogenesis in human SSc, we next clustered
195 scRNA-seq data for fibroblasts and identified ten sub-clusters across the datasets and
196 conditions (**Fig. 3A; fig. S5A**). Consistent with previous studies(*9*, *10*), we found the
197 corresponding fibroblast populations, including *SCARA5*$^+$/*PCOLCE2*$^+$/*LGR5*$^+$ fibroblasts
198 (Fib1), *MYOC*$^+$/*C3*$^+$/*APOD*$^+$ fibroblasts (Fib3), *CCL19*$^+$/*C7*$^+$/*APOE*$^+$ fibroblasts (Fib4),
199 *SFPR2*$^+$/*WIF1*/*APCDD1*$^+$ fibroblasts (Fib6), *COCH*$^+$/*SPARCL1*$^+$ fibroblasts (Fib7),
200 *COMP*$^+$/*SFPR2*$^+$/*PRSS23*$^+$ fibroblasts (Fib9), and *IGFBP2*$^+$/*ANGPTL7*$^+$ fibroblasts (Fib10)
201 (**Fig. 3B**). Moreover, Fib5 was characterized by the expression of *FOS*, *JUNB*, *JUN* and *FOSB*
202 which were components of activator protein 1 (AP1) known as the core transcription factors in
203 SSc fibrosis(*17*, *18*). Fib1 demonstrated the upregulation of *SCARA5*, which has been recently
204 identified as a marker for progenitor fibroblast in human myocardial and kidney fibrosis(*19*–
205 *21*). Fib2 and Fib9 were characterized by the expression of Periostin (*POSTN*), which encodes
206 an extracellular matrix protein that can amplify TGF-β signaling(*22*, *23*). In addition, Fib2 also
207 exhibited a high expression of myofibroblast hallmark *ACTA2* (**Fig. 3B**). Together, these
208 suggested that Fib2 and Fib9 as terminally-differentiated ECM-producing myofibroblasts.

209

210 Next, we compared the proportion of each sub-cluster between healthy and SSc samples. We
211 found that Fib1 showed a significant reduction in SSs skin (average fraction = 0.137) compared
212 to healthy skin (average fraction = 0.319) (p = 3.5e-10). In contrast, Fib2 exhibited an increase
213 in SSc skin (average fraction = 0.224) compared with that in healthy skin (average fraction =
214 0.114) (p = 5.7e-05) (**Fig. 3C**). We also estimated transcription factor (TF) activities for each
215 subset and observed that Fib2 was characterized by high TF activity of the hedgehog
216 transcription factor GLI2 (**fib. S5B**). This convergent driver can mediate Hedgehog pathways
217 in activating fibroblast and promoting fibrosis in SSc(*18*, *24*). Moreover, Fib9 was marked by
218 *SMAD3*, *SMAD4*, and *JUN*, all of which are TGF-β downstream pathways to promote fibrosis.
219 To validate our results, we re-analyzed a bulk RNA-seq dataset from *PRESS* cohort(*25*) and
220 observed the significant increase of *POSTN* and decrease of *SCARA5* in SSc skin compared
221 with healthy skin (**fib. S5C**). An inverse correlation was also observed in the gene expressions
222 between *SCARA5* and *POSTN* (**fig. S5C**). Overall, these findings further supported the potential
223 involvement of *SCARA5*$^+$ and *POSTN*$^+$ fibroblasts in the pathogenesis of SSc.

224

225 We next extended our analysis to spatial transcriptomics data. Visualization and quantification
226 of gene expression showed that *SCARA5* was significantly downregulated in SSc skin, whereas
227 *POSTN* was upregulated in SSc skin (**fig. S5D**). Additionally, *SCARA5* has exhibited distinct
228 spatial enrichment patterns that were mutually exclusive to regions enriched for *POSTN* and
229 *COMP* across multiple samples (**Fig. 3D and fig. S5E**). To characterize the spatial distribution
230 of fibroblast subsets, we calculated module scores of each subset, defined as the average
231 expression of the top 100 marker genes, across spatial spots based on their marker genes. This
232 analysis revealed that Fib2 and Fib9 were spatially colocalized (**Fig. 3E and fig. S5F**). To
233 probe the regulatory networks underlying these subsets, we estimated the activity of TFs and
234 signaling pathways, and observed increased activities of JUN, SMAD3, and the TGF-β
235 pathway, which were closely associated with the spatial localization of Fib2 and Fib9. These
236 findings align with their known pro-fibrotic roles, further confirming the spatial mapping of
237 these sub-clusters (**Figs. 3, F and G, figs. S5, G and H**). To explore the clinical relevance of
238 these findings, we correlated *SCARA5* and *POSTN* expression with clinical outcomes.
239 Interestingly, *SCARA5* expression negatively correlated with the mRSS, whereas *POSTN*
240 expression positively correlated with mRSS (**Fig. 3H**). Additionally, *SCARA5* showed an
241 inverse correlation with platelet counts, while *POSTN* negatively correlated with non-RP
242 disease duration. These results collectively suggested divergent effects of *SCARA5*$^+$ and
243 *POSTN*$^+$ fibroblasts in SSc fibrosis.

244

245 **Differentiation of *SCARA5*$^+$ to *POSTN*$^+$ fibroblasts in SSc skin**

246 While pioneering studies have identified *SCARA5*$^+$ fibroblasts as myofibroblast progenitors in
247 fibrosis[19–21], their differentiation trajectories have not been constructed yet. To firstly determine
248 if this phenomenon is consistent across different tissues such as SSc skin fibrosis, we analyzed
249 scRNA-seq data from mouse skin challenged by bleomycin (BLM) at various time points (days
250 3, 7, 14, and 28) and compared them to untreated skin (day 0, steady state)(*26*). This analysis
251 identified 14 distinct cell types and nine fibroblast sub-clusters (**figs. S6, A and B**). Among
252 these, we found a progressive decrease in *Scara5*$^+$ fibroblasts following BLM treatment, while
253 *Postn*$^+$ fibroblasts substantially increased on days 14 and 28 (**figs. S6, C and D**). These
254 temporal changes suggested a potential differentiation process from *Scara5*$^+$ to *Postn*$^+$
255 fibroblasts.

256

257 Based on these observations and the fact that Fib2 and Fib9 were marked by *POSTN*, we next
258 inferred two pseudo-time trajectories from Fib1 to Fib2 (trajectory 1) and Fib1 to Fib9
259 (trajectory 2) (**Fig3. I and J**). To characterize transcriptional dynamics during the
260 differentiation, we estimated the expression variation of each gene along the pseudo time and
261 identified 1524 and 1515 genes associated with trajectory 1 and 2, respectively. For trajectory
262 1, we found many genes were down-regulated during the differentiation, including precursor
263 marker *CD34(27)* and *SFRP2(9)* (**Fig. 3K, fig. S6E**). Moreover, we identified a set of genes,
264 including *C3*, *C7*, *CCL2*, and *CCL19*, that were particularly enriched at the intermediate stage
265 of the trajectory. This suggested a role for chemokine and cytokine signaling, as well as
266 complement system activity, in the differentiation process occurring at this stage. Genes
267 associated with the late stage of this trajectory include *FOS* and *JUNB,* which are involved in
268 the fibrosis-modulatory pathway and have been observed to be activated during the
269 myofibroblast transition process(*2*). For trajectory 2, we additionally observed that *TIMP2,*
270 *TGFBR3* and *APOD* were associated with the intermediate stage (**Fig. 3K, fig. S6F**). These
271 results revealed distinct gene regulatory networks that are involved in the divergent
272 differentiation of fibroblasts.

273

274 Of note, Sarthak Sinha et al conducted comparative single-cell multi-omics in reindeer
275 following full-thickness injury and found that the velvet skin regenerates, while the back skin
276 heals by forming a scar(*7*). Similarly, in reindeer skin, *SCARA5* gradually decreased but *ACTA2*
277 increased post wound in their back, but not in velvet (**figs. S7, A to E**). This pattern is
278 reminiscent of fibrotic tissue remodeling in human, which indicates the fibroblast dynamic
279 changes could be conserved across species and tissues.

280

281 **Spatial co-localization of fibroblast sub-clusters and other cell types**

282 Apart from highly discordant fibroblast states, the distinct stromal-immune linkages also
283 determine the fibrotic progression. Next, we investigated spatial dependencies between
284 fibroblast subsets and other major cell types to better understand their spatial communications
285 and contributions to fibrotic microenvironments. We conducted spatial colocalization analyses
286 in two distinct proximity areas: 1) co-occurrence within one single spot, determined by
287 Spearman correlation between the module score of each fibroblast sub-cluster and the
288 proportion of each major cell type, and 2) extended neighbourhood within an annular region
289 encompassing up to three surrounding spots for each target spot analyzed with the MlSTy

290 pipeline(*28*). The results from both approaches were averaged across all samples to identify
291 consistent spatial patterns. We focused specifically on Fib1, Fib2, and Fib9, as they have been
292 demonstrated to exhibit significant alterations in SSc (**Fig. 3C**). Notably, we observed a
293 consistent spatial dependency in both models across tissues, characterized by an increased co-
294 occurrence between fibroblast progenitor *SCARA5*$^{+}$ Fib1 and macrophages, whereas
295 *POSTN*$^{+}$/*ACTA2*$^{+}$ myofibroblasts (Fib2 and Fib9) were found in proximity to VSMCs (**Figs. 3,**
296 **L and M**). These findings point towards the potential critical role of macrophage in
297 establishing the spatial microenvironment surrounding fibroblast from the early stage.
298
299 **Correlations of the cellular phenotypes with clinical outcomes of SSc**
300 Next, we analyzed the potential correlations between the cellular phenotypes of fibroblast
301 subpopulations and their respective niches with the clinical outcomes and treatment
302 responsiveness in patients with SSc. The proportion of niche 0, which were predominantly
303 composed of fibroblasts and macrophages, were significantly higher in the SSc patients who
304 were non-responsive to a 52-week standard treatment of Mycophenolate mofetil (MMF),
305 compared to those who were responsive (median proportion in responder is 18.28%, n=5;
306 median proportion in non-responder is 25.00%, n=5, p=0.0079, determined by two-side
307 Wilcoxon rank sum test) (**Fig. 4A**). All the SSc patients included in our study have been under
308 the standard treatment of MMF for consecutive 52 weeks. The responsiveness was defined
309 according to the criteria of the revised ACR-CRISS (American College of Rheumatology
310 Composite Response Index in Systemic Sclerosis), which is the improvement in ≥ 3 of 5 core
311 clinical measurements with Minimal Clinically Important Difference (MCID) of 25% for
312 modified Rodnan skin score (mRSS), 5% for percent predicted forced vital capacity (FVC%),
313 20% for health assessment questionnaire-disability index (HAQ-DI), 20% for patient (PGA)
314 and clinician (CGA) global assessments(*29*). Consistently, the proportions of niche 0, which is
315 enriched with fibroblasts and characterized by high activity of TGF-β signaling, were
316 correlated negatively with *SCARA5*, and positively with *POSTN*, *ACTA2*, more pronounced
317 with the gene expression ratios of *POSTN/SCARA5*, and *ACTA2/SCARA5* (**Figs. 4, B to E**).
318 Moreover, the largely overlapping of Niche 0 and *POSTN*$^{+}$/*ACTA2*$^{+}$ myofibroblasts (Fib2 and
319 Fib9), as quantified by module scores based on the average expression of the top 100 marker
320 genes, which was observed by visualization using the ST data in SSc skin (**Fig. 4D**), which
321 indicates niche 0 was featured by the molecular phenotype of myofibroblast rather than
322 fibroblast progenitor. Furthermore, the ratios of *POSTN/SCARA5* and *ACTA2/SCARA5*
323 manifested the ability to discriminate the SSc patients from healthy controls with the AUC of

324 0.875 and 0.800 (p=0.0339 and 0.0897, respectively, **Fig. 4F**). Those baseline ratios were
325 observed to be significantly increased in the patients who experienced skin fibrosis progression
326 (**Fig. 4G**), determined as over 25% increment in mRSS assessed at 52-week follow-up. Notably,
327 the higher baseline ratios of *POSTN/SCARA5* and *ACTA2/SCARA5* were closely linked to the
328 non-responsiveness for the standard treatment with MMF for 52 weeks (**Fig. 4H**). These data
329 highlighted the potentials of aforementioned gene expression ratios in identification of the
330 standard-treatment-refractory SSc patients, who may require more advanced treatment
331 regimens rather than standard MMF. This provides insights into the future precision
332 stratification strategy for SSc patients.
333
334 **Characterization of macrophage heterogeneity**
335 We therefore asked how the immune microenvironment shapes the differentiation and
336 phenotypes of fibroblasts, and vice versa. Beyond the conventional polarization program of
337 macrophage, new subpopulations have been implicated in tissue fibrosis(*3–5*, *30*). They are not
338 the direct source of ECM, but rather a major source of immune dysregulation in fibrotic
339 conditions through release of proinflammatory and profibrotic factors(*31*). Nevertheless, the
340 heterogeneity of macrophages and their crosstalk with mesenchymal cells in the diseased
341 context of SSc remain poorly defined. We thus clustered the scRNA-seq data of macrophages
342 and identified three transcriptionally distinct subsets (**Fig. 5A, fig. S8A**). We observed one
343 cluster highly expressing proinflammatory cytokine *IL-1β*, as well as *CXCL8*, *CCL3*, *CXCL2*
344 and *PTGS2*, thus termed as proinflammatory macrophages (**Fig. 5B**). Recent studies have
345 suggested a role of IL-1β^+proinflammatory macrophages in idiopathic pulmonary fibrosis (IPF),
346 and in cardiac tissue remodeling(*3*, *4*). This subset also highly expresses members of the NR4A
347 subfamily of the nuclear hormone receptor superfamily including *NR4A3, NR4A2 and NR4A1*
348 (**Fig. 5B**), which have been identified as immediate early genes in response to various stimuli
349 and considered as promising therapeutic targets due to their significant roles in regulating
350 monocyte differentiation, macrophage activation and inflammatory response(*32*) and have
351 been linked to the pathogenesis of fibrotic tissue remodeling(*33*).
352
353 We also identified a sub-cluster characterized by phagocytic markers, including *MARCO*,
354 *LYVE1*, *CD36*, *FCGRT and C1QA*, therefore defined as phagocytic macrophages. The
355 scavenging receptor CD36, known to mediate uptake in macrophage, has been implicated in
356 the pathogenesis of tissue fibrosis(*34*, *35*). *MARCO*, a type II glycoprotein scavenger receptor
357 that binds a broad range of anionic ligands, was found to be upregulated in tissue-resident

358 macrophages and circulating monocytes upon activation. *MARCO*$^{+}$ myeloid cells have been
359 recognized as therapeutic targets for organ fibrosis in SSc(*36,37)*. LYVE1-expressing
360 macrophage has been demonstrated to form coordinated multi-cellular nest structures that are
361 distributed proximal to vasculature(*38*). Another subset of macrophage that may be involved
362 in the antigen presentation process is characterized by their overexpression of *HLA-B* and *HLA-*
363 *C,* hereafter referred to as antigen-presenting macrophages. Indeed, the antigen-presenting
364 macrophage and phagocytic macrophage defined here largely resembled previously identified
365 Lyve1^{lo}MHCII^{hi} and Lyve1^{hi}MHCII^{lo} macrophages, which are conserved across tissues(*8*).
366 Notably, the Lyve1^{hi}MHCII^{lo} macrophages have been demonstrated to play a critical role in
367 maintaining homeostasis, as depletion of Lyve1^{hi}MHCII^{lo} macrophages exacerbated
368 experimental lung and heart fibrosis, along with exacerbated vessel permeability, immune
369 infiltration and collagen deposition(*8*).

370 The comparison of cell proportion between healthy and SSc samples showed that
371 proinflammatory macrophages were significantly enriched in SSc (p = 0.0095), whereas the
372 abundance of phagocytic macrophages was significantly decreased in SSc samples (p = 0.027)
373 (**Fig. 5C**). We estimated TF activity for each cluster and observed a high activity of REL,
374 RELA, and RELB in proinflammatory macrophages (**fib. S8B**). These TFs are key members
375 of the NF-κB pathway that regulates immune and inflammatory responses(*39*), further
376 supporting the functions of proinflammatory macrophages.

377 **Crosstalk between fibroblast and macrophage sub-clusters**

378 Our analysis of ST data revealed a strong spatial association between macrophages and
379 fibroblasts, underscoring their potential functional interplay within the tissue
380 microenvironment (**Fig. 2C and Fig. 3L**). To further investigate the cellular crosstalk between
381 specific macrophage and fibroblast subtypes, we performed a detailed cell-cell communication
382 analysis using CellChat(*40*) in the scRNA-seq data based on ligand-receptor (L-R) interaction
383 networks. We retained only statistically significant L-R pairs between fibroblast and
384 macrophage sub-clusters, resulting in the identification of 393 distinct interactions. These
385 included 246 secreted autocrine/paracrine signaling interactions, 103 ECM-receptor
386 interactions, and 44 direct cell-cell contact-mediated interactions (**Fig. 5D**). This categorization
387 provides a comprehensive view of the diverse modes of communication utilized by these cell
388 types to orchestrate their roles in the tissue microenvironment. Among macrophage subsets,
389 pro-inflammatory macrophages exhibited the highest number of interactions with fibroblast

390 subsets (n = 179 interactions), suggesting that they are central players in fibroblast-mediated
391 signaling (**Fig. 5E**). Particularly, Fib9 emerged as a key fibroblast subtype with the strongest
392 connectivity to macrophages (n = 83 interactions), outpacing other fibroblast subsets in its
393 interaction capacity.
394
395 Visualization of the specific L-R interactions revealed that macrophages receive signals from
396 fibroblasts through multiple signaling pathways, including THBS, MIF, CXCL, LAMININ,
397 and COLLAGEN (**fig. S8C**). Among these interactions, the receptor CXCR4 was observed to
398 interact with fibroblast-derived ligands such as MIF and CXCL12. This interaction suggests a
399 mechanism by which fibroblasts recruit and retain proinflammatory macrophages, thereby
400 sustaining local inflammation and contributing to the progression of fibrosis (**Fig. 5F**). On the
401 other hand, fibroblasts also acted as signal receivers, engaging the receptor ACKR3 to interact
402 with MIF and CXCL12 (**fig. S8D and Fig. 5G**). Notably, *MIF* and *CXCL12* were expressed
403 by nearly all subtypes of fibroblasts and macrophages (**Figs. 5, H and I**), underscoring their
404 widespread involvement in cellular crosstalk.
405
406 However, the expression of *CXCR4* was specific to proinflammatory macrophages, while
407 *ACKR3* was uniquely expressed in the Fib1 fibroblast progenitor subcluster (**Fig. 5H**). To
408 confirm at the protein levels, we applied Tyramide Signal Amplification (TSA) high-plex
409 immunofluorescence onto adjacent tissue sections. Our TSA staining confirmed the
410 overlapping expression of ACKR3 in *SCARA5*$^{+}$ fibroblast (**Fig. 5J**). Again, we observed IL-
411 1β^{+} macrophages, which were also positive for CXCR4, closely distributed adjacent to
412 fibroblasts (**Fig. 5K**). Together, these results revealed a highly organized and reciprocal
413 signaling network between fibroblasts and macrophages, underscored by distinct L-R
414 interactions. Of particular interest, the chemokine CXCL12 can bind to its classic receptor
415 CXCR4, a G protein-coupled receptor, facilitating the recruitment of CXCR4^{+} cells, such as
416 proinflammatory macrophages in our case. Alternatively, CXCL12 can interact with its
417 atypical chemokine receptor ACKR3 independent of GPCR mediated signaling. ACKR3 is
418 capable of actively internalizing its chemokine ligands CXCL12, through scavenging. This
419 function helps to modulate the availability and gradient of CXCL12 in the extracellular
420 environment(*41*). The selective expression of ACKR3 in fibroblast progenitors may indicate
421 an endogenous compensation at an early stage. A dysfunction in this mechanism could lead to
422 the subsequent CXCR4 mediated recruitment of macrophages, during the transition from
423 fibroblast progenitor to myofibroblast over the course of SSc progression.

424

425 **A data-driven model of SSc**

426 Taken together, we proposed a data-driven disease model of SSc based on the results of multi-
427 omics data obtained from SSc, a prototypical systemic fibrotic condition (**Fig. 6**). An imbalance
428 in fibroblast subsets in SSc was characterized by a decrease in *SCARA5*$^{+}$ fibroblast progenitors
429 and an increase in *POSTN*$^{+}$ and *ACTA2*$^{+}$ terminally differentiated myofibroblasts, which
430 promote the excessive ECM deposition. The decreased phagocytic macrophages
431 (Lyve1^{hi}MHCII^{lo}) may contribute to the impairment of vessel integrity. The infiltration of
432 proinflammatory macrophages (IL-1β^{+}) was observed actively interact with fibroblast subsets.
433 These proinflammatory macrophages were overexpressed with *CXCR4*, which may mediate
434 their recruitment by interacting with *CXCL12*. Additionally, the expression of ACKR3 on
435 fibroblasts, particularly in progenitors under homeostatic conditions, may regulate the local
436 levels CXCL12 by internalizing the ligand, thereby limiting excessive leukocyte recruitment
437 and preventing unwanted tissue inflammation. However, this regulatory mechanism might
438 diminish in effectiveness as progenitor fibroblasts decrease during the progression of SSc,
439 ultimately resulting in uncontrolled CXCL12/CXCR4-mediated inflammatory cell attraction.
440 This regulatory network fosters a shift from tissue homeostasis to a fibrogenic state, driving
441 the progression of SSc. Therefore, the integration of spatial omics with scRNA-seq provides
442 insight into the immune-stromal crosstalk involved in the pathogenesis of SSc.

443

444 **DISCUSSION**

445 SSc is a multifaceted autoimmune disease characterized by a well-known triad of
446 manifestations: vasculopathy, autoimmunity and fibrosis. In this study, we provided a
447 comprehensive map of the skin ecosystem in SSc using genome-wide spatial transcriptomes
448 based on 10x Visium and Stereo-seq platforms combined with additional scRNA-seq datasets.
449 We identified disease-associated fibroblasts and macrophages and characterized their intricate
450 interplay within niches that potentially drive the transition from a homeostatic to a fibrogenic
451 state. The molecular signatures of cell populations were validated through spatial proteomics,
452 including IMC and TSA. The differentiation trajectory of fibroblasts was cross-validated using
453 time-course bleomycin induced SSc mouse and wound-healing reindeer models. Further
454 investigation into cell-cell communications offered potential for identifying targetable disease-
455 driving molecules for therapeutic intervention.

456

457 We identified distinct niches enriched with fibroblasts and macrophages, showing active TGF-
458 β signaling pathway and correlating with clinical outcomes in SSc. We then homed in on
459 distinct cell phenotypes and spatial relationships of fibroblasts and macrophages within niches.
460 Of note, we discovered a proportional imbalance of fibroblast subsets in SSc, with a clear
461 reduction in SCARA5^{+} progenitor fibroblast and an upregulation in *POSTN*$^{+}$/*ACTA2*$^{+}$
462 terminally differentiated myofibroblasts compared with healthy controls. SCARA5 positive
463 fibroblasts have been recently reported as myofibroblast progenitors in heart and kidney(*19*,
464 *20*, *42*). A cross-tissue human fibroblast atlas, derived from 517 human samples encompassing
465 11 tissue types and diverse pathological states, demonstrated the substantial overlaps among
466 *SCARA5*$^{+}$ fibroblast and progenitor-like fibroblast, as well as between *POSTN*$^{+}$ fibroblast and
467 myofibroblast(*43*). Additionally, the dynamic changes of fibroblasts were not only identified
468 through trajectory analysis in human SSc skin, but also validated in time-course models of SSc
469 mouse and wound-healing reindeer using the publicly available datasets(*7*, *26*). These findings
470 indicated that the differentiation from *SCARA5*$^{+}$ fibroblast progenitors to myofibroblasts
471 represents a conserved phenotype across different tissues and species. Targeting the shared
472 mechanism has emerged as a strategy for basket trial design especially for rare diseases that
473 share the same triggering or perpetuating signaling pathways, such as INBUILD study(*44*).
474
475 Importantly, our data revealed the baseline gene expression ratios of marker genes for
476 myofibroblast versus fibroblast progenitor indicate progression in skin fibrosis and an
477 incomplete response to standard treatment, assessed using a composite responsiveness
478 criteria(*29*) based on clinically significant changes at 52-week follow-up. Pretreatment
479 stratification of SSc patients using expression ratios revealing dynamic changes in fibroblast
480 states underscores its vital role in precision medicine for predicting treatment response
481 likelihood. Furthermore, future studies are necessary to elucidate the spatiotemporal changes
482 occurring within fibrogeneis microenvironment by examining longitudinal biopsies throughout
483 the trajectory of the disease and during treatment.
484
485 Of note, we revealed an intense interaction between IL-1β^{+} proinflammatory macrophages and
486 fibroblast subsets in SSc. Infiltrating macrophages activate fibroblasts by secreting IL-1β,
487 whilst systemic IL-1β inhibition or targeted IL-1β deletion in macrophages prevents fibroblast
488 activation(*3*, *4*, *45*). Furthermore, we found this crosstalk was predicted to be mediated by the
489 interaction of CXCL12 with CXCR4 in macrophages and ACKR3 in fibroblast progenitors.
490 Indeed, we also found the deregulation of Lyve1^{hi}MHCII^{lo} macrophages in SSc, which are

491 known to play a protective role by maintaining vascular integrity and preventing immune cell
492 infiltration in fibrotic conditions(*8*). These sequential events such as tissue entry and immune
493 infiltration occuring in SSc may shift the hemostatic condition towards a profibrotic
494 environment. Importantly, the inability to constrain CXCL12 overexpression in the milieu
495 through internalization by fibroblast progenitors via ACKR3 leads to CXCR4-mediated
496 proinflammatory macrophage recruitment, which is reflective of the fine-tuned regulation by
497 local fibroblasts.
498
499 Our research aimed to explore the potential to halt the disease progression by interrupting the
500 crosstalk between pathological cells. Spatial transcriptomics provides a unique advantage in
501 examining the structured compartment and the cellular composition and states within specific
502 microenvironments. However, the 10x Visium platform does hold significant limitations, such
503 as the low resolution of 55-um per spot. To overcome this limitation and increase granularity,
504 we employed a higher-resolution spatial transcriptomics technology, FFPE-based Stereo-seq,
505 achieving a resolution of 0.5 um per spot. To further validate the genome-wide spatial data, we
506 applied additionally spatial proteomics, including IMC and TSA, which offering the molecular
507 expression and distribution of the identified cells in SSc skin at single-cell level with the
508 resolutions of 1 um^2 and 0.25 um^2 per pixel, respectively. To achieve a comprehensive
509 description of the skin landscape in SSc, we also recognize that three-dimensional profiling of
510 tissue space and subcellular localization of protein signals will significantly expand our
511 understanding in SSc pathogenesis.

512 In summary, spatial multi-omics combined with scRNA-seq helps to elucidate the
513 entanglement of fibroblasts and macrophages, forming a connectivity network in the
514 pathogenesis of SSc. Within this network, fibroblasts and macrophages with distinct
515 phenotypes contribute to tissue fibrotic remodeling in a coordinated manner. We thus used this
516 strategy to facilitate target discovery, identifying potential intervention axes for fibrosis.

517

518 **MATERIALS AND METHODS**

519

520 **Study Design**

521 The objective of this study was to unbiasedly characterize the cellular niche and neighbourhood
522 interaction driving SSc fibrosis, providing spatiotemporal insights into potential target

523 identification and precise stratification. We thus obtained skin punch biopsy samples from
524 patients with patients with early and diffuse cutaneous involvement of SSc, and as well as from
525 healthy controls. We generated spatially resolved transcriptome maps using two
526 complementary spatial technologies: 10x Visium and Stereo-seq (spatial enhanced resolution
527 omics sequencing). By integrating these datasets with publicly available scRNA-seq datasets,
528 we constructed a population-scale human skin transcriptome atlas, which enabled us to study
529 the cellular and molecular landscape of SSc with spatial resolution. We then conducted the
530 subsequent analyses, including cell-type deconvolution, tissue structure identification, disease-
531 associated subclustering, trajectory analysis, spatial colocalization, and ligand-receptor
532 analysis. The findings were validated using spatial proteomic techniques such as imaging mass
533 cytometry (IMC) and tyramide signal amplification (TSA), as well as time-course scRNA-seq
534 data of SSc mouse and wound-healing reindeer models. Furthermore, we analyzed the
535 associations of these findings with clinical outcomes and treatment responsiveness in SSc (**Fig.
536 1A**).
537

538 **Further details on Materials and Methods can be found in the Supplementary Materials.**

539

540 **List of Supplementary Materials**

541 Supplementary Materials and Methods
542 Fig. S1: Quality check of spatial transcriptomics data.
543 Fig. S2: Analysis of publicly available scRNA-seq data.
544 Fig. S3: Characterization of cell-type niches in human skin.
545 Fig. S4: Validation of cellular neighbourhood (CN) by imaging mass cytometry (IMC) in
546 healthy and SSc skin.
547 Fig. S5: Sub-clustering of fibroblasts.
548 Fig. S6: Trajectory analysis of fibroblast differentiation.
549 Fig. S7: Cross-Species Validation of Fibroblast Dynamics.
550 Fig. S8: Sub-clustering of macrophages.
551 Table. S1: Clinical characterization of the patients with SSc undergoing skin biopsy for spatial
552 transcriptomic study.
553 Table. S2: Quality statistics for 10x Visium and Stereo-seq data.
554

References (46~55 for Supplementary Materials)

1. M. Elhai, C. Meune, M. Boubaya, J. Avouac, E. Hachulla, A. Balbir-Gurman, G. Riemekasten, P. Airò, B. Joven, S. Vettori, F. Cozzi, S. Ullman, L. Czirják, M. Tikly, U. Müller-Ladner, P. Caramaschi, O. Distler, F. Iannone, L. P. Ananieva, R. Hesselstrand, R. Becvar, A. Gabrielli, N. Damjanov, M. J. Salvador, V. Riccieri, C. Mihai, G. Szücs, U. A. Walker, N. Hunzelmann, D. Martinovic, V. Smith, C. de S. Müller, C. M. Montecucco, D. Opris, F. Ingegnoli, P. G. Vlachoyiannopoulos, B. Stamenkovic, E. Rosato, S. Heitmann, J. H. W. Distler, T. Zenone, M. Seidel, A. Vacca, E. D. Langhe, S. Novak, M. Cutolo, L. Mouthon, J. Henes, C. Chizzolini, C. A. von Mühlen, K. Solanki, S. Rednic, L. Stamp, B. Anic, V. O. Santamaria, M. De Santis, S. Yavuz, W. A. Sifuentes-Giraldo, E. Chatelus, J. Stork, J. van Laar, E. Loyo, P. García de la Peña Lefebvre, K. Eyerich, V. Cosentino, J. J. Alegre-Sancho, O. Kowal-Bielecka, G. Rey, M. Matucci-Cerinic, Y. Allanore, EUSTAR group, Mapping and predicting mortality from systemic sclerosis. *Ann. Rheum. Dis.* **76**, 1897–1905 (2017).

2. J. H. W. Distler, A.-H. Györfi, M. Ramanujam, M. L. Whitfield, M. Königshoff, R. Lafyatis, Shared and distinct mechanisms of fibrosis. *Nat. Rev. Rheumatol.* **15**, 705–730 (2019).

3. M. Alexanian, A. Padmanabhan, T. Nishino, J. G. Travers, L. Ye, A. Pelonero, C. Y. Lee, N. Sadagopan, Y. Huang, K. Auclair, A. Zhu, Y. An, C. A. Ekstrand, C. Martinez, B. G. Teran, W. R. Flanigan, C. K.-S. Kim, K. Lumbao-Conradson, Z. Gardner, L. Li, M. W. Costa, R. Jain, I. Charo, A. J. Combes, S. M. Haldar, K. S. Pollard, R. J. Vagnozzi, T. A. McKinsey, P. F. Przytycki, D. Srivastava, Chromatin remodelling drives immune cell-fibroblast communication in heart failure. *Nature* **635**, 434–443 (2024).

4. J. M. Amrute, X. Luo, V. Penna, S. Yang, T. Yamawaki, S. Hayat, A. Bredemeyer, I.-H. Jung, F. F. Kadyrov, G. S. Heo, R. Venkatesan, S. Y. Shi, A. Parvathaneni, A. L. Koenig, C. Kuppe, C. Baker, H. Luehmann, C. Jones, B. Kopecky, X. Zeng, T. Bleckwehl, P. Ma, P. Lee, Y. Terada, A. Fu, M. Furtado, D. Kreisel, A. Kovacs, N. O. Stitziel, S. Jackson, C.-M. Li, Y. Liu, N. A. Rosenthal, R. Kramann, B. Ason, K. J. Lavine, Targeting immune-fibroblast cell communication in heart failure. *Nature* **635**, 423–433 (2024).

5. C. H. Mayr, D. Santacruz, S. Jarosch, M. Bleck, J. Dalton, A. McNabola, C. Lempp, L. Neubert, B. Rath, J. C. Kamp, D. Jonigk, M. Kühnel, H. Schlüter, A. Klimowicz, J. Doerr,

586 A. Dick, F. Ramirez, M. J. Thomas, Spatial transcriptomic characterization of pathologic
587 niches in IPF. *Sci. Adv.* **10**, eadl5473 (2024).

588 6. C. Morse, T. Tabib, J. Sembrat, K. L. Buschur, H. T. Bittar, E. Valenzi, Y. Jiang, D. J.
589 Kass, K. Gibson, W. Chen, A. Mora, P. V. Benos, M. Rojas, R. Lafyatis, Proliferating
590 SPP1/MERTK-expressing macrophages in idiopathic pulmonary fibrosis. *Eur. Respir. J.*
591 **54**, 1802441 (2019).

592 7. S. Sinha, H. D. Sparks, E. Labit, H. N. Robbins, K. Gowing, A. Jaffer, E. Kutluberk, R.
593 Arora, M. S. B. Raredon, L. Cao, S. Swanson, P. Jiang, O. Hee, H. Pope, M. Workentine,
594 K. Todkar, N. Sharma, S. Bharadia, K. Chockalingam, L. G. N. de Almeida, M. Adam, L.
595 Niklason, S. S. Potter, A. W. Seifert, A. Dufour, V. Gabriel, N. L. Rosin, R. Stewart, G.
596 Muench, R. McCorkell, J. Matyas, J. Biernaskie, Fibroblast inflammatory priming
597 determines regenerative versus fibrotic skin repair in reindeer. *Cell* **185**, 4717–4736.e25
598 (2022).

599 8. S. Chakarov, H. Y. Lim, L. Tan, S. Y. Lim, P. See, J. Lum, X.-M. Zhang, S. Foo, S.
600 Nakamizo, K. Duan, W. T. Kong, R. Gentek, A. Balachander, D. Carbajo, C. Bleriot, B.
601 Malleret, J. K. C. Tam, S. Baig, M. Shabeer, S.-A. E. S. Toh, A. Schlitzer, A. Larbi, T.
602 Marichal, B. Malissen, J. Chen, M. Poidinger, K. Kabashima, M. Bajenoff, L. G. Ng, V.
603 Angeli, F. Ginhoux, Two distinct interstitial macrophage populations coexist across
604 tissues in specific subtissular niches. *Science* **363**, eaau0964 (2019).

605 9. T. Tabib, M. Huang, N. Morse, A. Papazoglou, R. Behera, M. Jia, M. Bulik, D. E. Monier,
606 P. V. Benos, W. Chen, R. Domsic, R. Lafyatis, Myofibroblast transcriptome indicates
607 SFRP2hi fibroblast progenitors in systemic sclerosis skin. *Nat. Commun.* **12**, 4384 (2021).

608 10. C. Gur, S.-Y. Wang, F. Sheban, M. Zada, B. Li, F. Kharouf, H. Peleg, S. Aamar, A. Yalin,
609 D. Kirschenbaum, Y. Braun-Moscovici, D. A. Jaitin, T. Meir-Salame, E. Hagai, B. K.
610 Kragesteen, B. Avni, S. Grisariu, C. Bornstein, S. Shlomi-Loubaton, E. David, R.
611 Shreberk-Hassidim, V. Molho-Pessach, D. Amar, T. Tzur, R. Kuint, M. Gross, O. Barboy,
612 A. Moshe, L. Fellus-Alyagor, D. Hirsch, Y. Addadi, S. Erenfeld, M. Biton, T. Tzemach,
613 A. Elazary, Y. Naparstek, R. Tzemach, A. Weiner, A. Giladi, A. Balbir-Gurman, I. Amit,
614 LGR5 expressing skin fibroblasts define a major cellular hub perturbed in scleroderma.
615 *Cell* **185**, 1373–1388.e20 (2022).

616 11. K. E. N. Clark, S. Xu, M. Attah, V. H. Ong, C. D. Buckley, C. P. Denton, Single-cell
617 analysis reveals key differences between early-stage and late-stage systemic sclerosis skin
618 across autoantibody subgroups. *Ann. Rheum. Dis.* **82**, 1568–1579 (2023).

619 12. H. Yin, O. Distler, L. Shen, X. Xu, Y. Yuan, R. Li, B. Liu, Q. Li, Q. Huang, F. Xie, Z.
620 Zhang, R. Liang, X. Dai, X. Chen, B. Li, Q. Yan, L. Lu, Endothelial response to type I
621 interferon contributes to vasculopathy and fibrosis and predicts disease progression of
622 systemic sclerosis. *Arthritis Rheumatol.* **76**, 78–91 (2024).

623 13. F. Ma, P.-S. Tsou, M. Gharaee-Kermani, O. Plazyo, X. Xing, J. Kirma, R. Wasikowski,
624 G. A. Hile, P. W. Harms, Y. Jiang, E. Xing, M. Nakamura, D. Ochocki, W. D. Brodie, S.
625 Pillai, E. Maverakis, M. Pellegrini, R. L. Modlin, J. Varga, L. C. Tsoi, R. Lafyatis, J. M.
626 Kahlenberg, A. C. Billi, D. Khanna, J. E. Gudjonsson, Systems-based identification of the
627 Hippo pathway for promoting fibrotic mesenchymal differentiation in systemic sclerosis.
628 *Nat. Commun.* **15**, 210 (2024).

629 14. A. Rius Rigau, M. Liang, V. Devakumar, R. Neelagar, A.-E. Matei, A.-H. Györfi, C.
630 Bergmann, T. Filla, V. Fedorchenko, G. Schett, J. H. W. Distler, Y.-N. Li, Imaging mass
631 cytometry-based characterisation of fibroblast subsets and their cellular niches in systemic
632 sclerosis. *Ann. Rheum. Dis.*, doi: 10.1136/ard-2024-226336 (2024).

633 15. A. Rius Rigau, Y.-N. Li, A.-E. Matei, A.-H. Györfi, P.-M. Bruch, S. Koziel, V.
634 Devakumar, A. Gabrielli, A. Kreuter, J. Wang, S. Dietrich, G. Schett, J. H. W. Distler, M.
635 Liang, Characterization of vascular niche in systemic sclerosis by spatial proteomics. *Circ.*
636 *Res.* **134**, 875–891 (2024).

637 16. A. Chen, S. Liao, M. Cheng, K. Ma, L. Wu, Y. Lai, X. Qiu, J. Yang, J. Xu, S. Hao, X.
638 Wang, H. Lu, X. Chen, X. Liu, X. Huang, Z. Li, Y. Hong, Y. Jiang, J. Peng, S. Liu, M.
639 Shen, C. Liu, Q. Li, Y. Yuan, X. Wei, H. Zheng, W. Feng, Z. Wang, Y. Liu, Z. Wang, Y.
640 Yang, H. Xiang, L. Han, B. Qin, P. Guo, G. Lai, P. Muñoz-Cánoves, P. H. Maxwell, J. P.
641 Thiery, Q.-F. Wu, F. Zhao, B. Chen, M. Li, X. Dai, S. Wang, H. Kuang, J. Hui, L. Wang,
642 J.-F. Fei, O. Wang, X. Wei, H. Lu, B. Wang, S. Liu, Y. Gu, M. Ni, W. Zhang, F. Mu, Y.
643 Yin, H. Yang, M. Lisby, R. J. Cornall, J. Mulder, M. Uhlén, M. A. Esteban, Y. Li, L. Liu,
644 X. Xu, J. Wang, Spatiotemporal transcriptomic atlas of mouse organogenesis using DNA
645 nanoball-patterned arrays. *Cell* **185**, 1777–1792.e21 (2022).

646 17. J. Avouac, K. Palumbo, M. Tomcik, P. Zerr, C. Dees, A. Horn, B. Maurer, A.
647 Akhmetshina, C. Beyer, A. Sadowski, H. Schneider, S. Shiozawa, O. Distler, G. Schett,
648 Y. Allanore, J. H. W. Distler, Inhibition of activator protein 1 signaling abrogates
649 transforming growth factor β-mediated activation of fibroblasts and prevents experimental
650 fibrosis. *Arthritis Rheum.* **64**, 1642–1652 (2012).

651 18. C. Bergmann, S. Chenguiti Fakhouri, T.-M. Thuong, T. Filla, A. R. Rigau, A. B. Ekici, B.
652 Merlevede, L. Hallenberger, H. Zhu, C. Dees, A.-E. Matei, J. Auth, A.-H. Györfi, X. Zhou,
653 S. Rauber, A. Bozec, N. Dickel, C. Liang, M. Kunz, G. Schett, J. H. W. Distler, Mutual
654 amplification of GLI2/Hedgehog and cJUN/AP1 signaling in fibroblasts in Systemic
655 Sclerosis (SSc) - potential implications for combined therapies. *Arthritis Rheumatol.*, doi:
656 10.1002/art.42979 (2024).

657 19. C. Kuppe, M. M. Ibrahim, J. Kranz, X. Zhang, S. Ziegler, J. Perales-Patón, J. Jansen, K.
658 C. Reimer, J. R. Smith, R. Dobie, J. R. Wilson-Kanamori, M. Halder, Y. Xu, N. Kabgani,
659 N. Kaesler, M. Klaus, L. Gernhold, V. G. Puelles, T. B. Huber, P. Boor, S. Menzel, R. M.
660 Hoogenboezem, E. M. J. Bindels, J. Steffens, J. Floege, R. K. Schneider, J. Saez-
661 Rodriguez, N. C. Henderson, R. Kramann, Decoding myofibroblast origins in human
662 kidney fibrosis. *Nature* **589**, 281–286 (2021).

663 20. C. Kuppe, R. O. Ramirez Flores, Z. Li, S. Hayat, R. T. Levinson, X. Liao, M. T. Hannani,
664 J. Tanevski, F. Wünnemann, J. S. Nagai, M. Halder, D. Schumacher, S. Menzel, G.
665 Schäfer, K. Hoeft, M. Cheng, S. Ziegler, X. Zhang, F. Peisker, N. Kaesler, T. Saritas, Y.
666 Xu, A. Kassner, J. Gummert, M. Morshuis, J. Amrute, R. J. A. Veltrop, P. Boor, K. Klingel,
667 L. W. Van Laake, A. Vink, R. M. Hoogenboezem, E. M. J. Bindels, L. Schurgers, S.
668 Sattler, D. Schapiro, R. K. Schneider, K. Lavine, H. Milting, I. G. Costa, J. Saez-
669 Rodriguez, R. Kramann, Spatial multi-omic map of human myocardial infarction. *Nature*
670 **608**, 766–777 (2022).

671 21. Z. Li, C. Kuppe, S. Ziegler, M. Cheng, N. Kabgani, S. Menzel, M. Zenke, R. Kramann, I.
672 G. Costa, Chromatin-accessibility estimation from single-cell ATAC-seq data with
673 scOpen. *Nat. Commun.* **12**, 6386 (2021).

674 22. Y. Nanri, S. Nunomura, Y. Terasaki, T. Yoshihara, Y. Hirano, Y. Yokosaki, Y.
675 Yamaguchi, C. Feghali-Bostwick, K. Ajito, S. Murakami, S. J. Conway, K. Izuhara,
676 Cross-talk between transforming growth factor-β and periostin can be targeted for

677 pulmonary fibrosis. *Am. J. Respir. Cell Mol. Biol.* **62**, 204–216 (2020).

678 23. Y. Nanri, S. Nunomura, Y. Honda, H. Takedomi, Y. Yamaguchi, K. Izuhara, A positive
679 loop formed by SOX11 and periostin upregulates TGF-β signals leading to skin fibrosis.
680 *J. Invest. Dermatol.* **143**, 989–998.e7 (2023).

681 24. R. Liang, B. Šumová, C. Cordazzo, T. Mallano, Y. Zhang, T. Wohlfahrt, C. Dees, A.
682 Ramming, D. Krasowska, M. Michalska-Jakubus, O. Distler, G. Schett, L. Šenolt, J. H.
683 W. Distler, The transcription factor GLI2 as a downstream mediator of transforming
684 growth factor-β-induced fibroblast activation in SSc. *Ann. Rheum. Dis.* **76**, 756–764
685 (2017).

686 25. B. Skaug, D. Khanna, W. R. Swindell, M. E. Hinchcliff, T. M. Frech, V. D. Steen, F. N.
687 Hant, J. K. Gordon, A. A. Shah, L. Zhu, W. J. Zheng, J. L. Browning, A. M. S. Barron,
688 M. Wu, S. Visvanathan, P. Baum, J. M. Franks, M. L. Whitfield, V. K. Shanmugam, R.
689 T. Domsic, F. V. Castelino, E. J. Bernstein, N. Wareing, M. A. Lyons, J. Ying, J. Charles,
690 M. D. Mayes, S. Assassi, Global skin gene expression analysis of early diffuse cutaneous
691 systemic sclerosis shows a prominent innate and adaptive inflammatory profile. *Ann.*
692 *Rheum. Dis.* **79**, 379–386 (2020).

693 26. Y. Liang, Y. Hu, J. Zhang, H. Song, X. Zhang, Y. Chen, Y. Peng, L. Sun, Y. Sun, R. Xue,
694 S. Ji, C. Li, Z. Rong, B. Yang, Y. Xu, Dynamic pathological analysis reveals a protective
695 role against skin fibrosis for TREM2-dependent macrophages. *Theranostics* **14**, 2232–
696 2245 (2024).

697 27. B. Nazari, L. M. Rice, G. Stifano, A. M. S. Barron, Y. M. Wang, T. Korndorf, J. Lee, J.
698 Bhawan, R. Lafyatis, J. L. Browning, Altered dermal fibroblasts in systemic sclerosis
699 display podoplanin and CD90. *Am. J. Pathol.* **186**, 2650–2664 (2016).

700 28. J. Tanevski, R. O. R. Flores, A. Gabor, D. Schapiro, J. Saez-Rodriguez, Explainable
701 multiview framework for dissecting spatial relationships from highly multiplexed data.
702 *Genome Biol.* **23**, 97 (2022).

703 29. D. Khanna, S. Huang, C. J. F, Lin, C. Spino. New Composite Endpoint Early Diffuse
704 Cutaneous Systemic Sclerosis-Revisiting Provisional American College Rheumatology
705 Composite Response Index Systemic Sclerosis.*Ann Rheum Dis*. 80, 641-650 (2021).

706 30. M. B. Buechler, W. Fu, S. J. Turley, Fibroblast-macrophage reciprocal interactions in
707 health, fibrosis, and cancer. *Immunity* **54**, 903–915 (2021).

708 31. R. Bhandari, M. S. Ball, V. Martyanov, D. Popovich, E. Schaafsma, S. Han, M.
709 ElTanbouly, N. M. Orzechowski, M. Carns, E. Arroyo, K. Aren, M. Hinchcliff, M. L.
710 Whitfield, P. A. Pioli, Profibrotic activation of human macrophages in systemic sclerosis.
711 *Arthritis Rheumatol.* **72**, 1160–1169 (2020).

712 32. S. Boulet, L. Le Corre, L. Odagiu, N. Labrecque, Role of NR4A family members in
713 myeloid cells and leukemia. *Curr. Res. Immunol.* **3**, 23–36 (2022).

714 33. K. Palumbo-Zerr, P. Zerr, A. Distler, J. Fliehr, R. Mancuso, J. Huang, D. Mielenz, M.
715 Tomcik, B. G. Fürnrohr, C. Scholtysek, C. Dees, C. Beyer, G. Krönke, D. Metzger, O.
716 Distler, G. Schett, J. H. W. Distler, Orphan nuclear receptor NR4A1 regulates
717 transforming growth factor-β signaling and fibrosis. *Nat. Med.* **21**, 150–158 (2015).

718 34. D. Kwak, P. B. Bradley, N. Subbotina, S. Ling, S. Teitz-Tennenbaum, J. J. Osterholzer,
719 T. H. Sisson, K. K. Kim, CD36/Lyn kinase interactions within macrophages promotes
720 pulmonary fibrosis in response to oxidized phospholipid. *Respir. Res.* **24**, 314 (2023).

721 35. S. Pennathur, K. Pasichnyk, N. M. Bahrami, L. Zeng, M. Febbraio, I. Yamaguchi, D. M.
722 Okamura, The macrophage phagocytic receptor CD36 promotes fibrogenic pathways on
723 removal of apoptotic cells during chronic kidney injury. *Am. J. Pathol.* **185**, 2232–2245
724 (2015).

725 36. A. Papazoglou, M. Huang, M. Bulik, A. Lafyatis, T. Tabib, C. Morse, J. Sembrat, M.
726 Rojas, E. Valenzi, R. Lafyatis, Epigenetic regulation of profibrotic macrophages in
727 systemic sclerosis-associated interstitial lung disease. *Arthritis Rheumatol.* **74**, 2003–2014
728 (2022).

729 37. D. Xu, S. Bhattacharyya, W. Wang, I. Ifergan, M.-Y. A. C. Wong, D. Procissi, A.
730 Yeldandi, S. Bale, R. G. Marangoni, C. Horbinski, S. D. Miller, J. Varga, PLG
731 nanoparticles target fibroblasts and MARCO+ monocytes to reverse multiorgan fibrosis.
732 *JCI Insight* **7** (2022).

733 38. J. E. Anstee, K. T. Feehan, J. W. Opzoomer, I. Dean, H. P. Muller, M. Bahri, T. S. Cheung,
734 K. Liakath-Ali, Z. Liu, D. Choy, J. Caron, D. Sosnowska, R. Beatson, T. Muliaditan, Z.

735 An, C. E. Gillett, G. Lan, X. Zou, F. M. Watt, T. Ng, J. M. Burchell, S. Kordasti, D. R.
736 Withers, T. Lawrence, J. N. Arnold, LYVE-1+ macrophages form a collaborative CCR5-
737 dependent perivascular niche that influences chemotherapy responses in murine breast
738 cancer. *Dev. Cell* **58**, 1548–1561.e10 (2023).

739 39. T. Liu, L. Zhang, D. Joo, S.-C. Sun, NF-κB signaling in inflammation. *Signal Transduct.*
740 *Target. Ther.* **2** (2017).

741 40. S. Jin, M. V. Plikus, Q. Nie, CellChat for systematic analysis of cell-cell communication
742 from single-cell transcriptomics. *Nat. Protoc.*, doi: 10.1038/s41596-024-01045-4 (2024).

743 41. G. Cuesta-Margolles, G. Schlecht-Louf, F. Bachelerie, ACKR3 in skin homeostasis, an
744 overlooked player in the CXCR4/CXCL12 axis. *J. Invest. Dermatol.*, doi:
745 10.1016/j.jid.2024.08.022 (2024).

746 42. F. Schreibing, T. M. Anslinger, R. Kramann, Fibrosis in pathology of heart and kidney:
747 From deep RNA-sequencing to novel molecular targets. *Circ. Res.* **132**, 1013–1033 (2023).

748 43. Y. Gao, J. Li, W. Cheng, T. Diao, H. Liu, Y. Bo, C. Liu, W. Zhou, M. Chen, Y. Zhang, Z.
749 Liu, W. Han, R. Chen, J. Peng, L. Zhu, W. Hou, Z. Zhang, Cross-tissue human fibroblast
750 atlas reveals myofibroblast subtypes with distinct roles in immune modulation. *Cancer*
751 *Cell* **42**, 1764–1783.e10 (2024).

752 44. K. R. Flaherty, A. U. Wells, V. Cottin, A. Devaraj, S. L. F. Walsh, Y. Inoue, L. Richeldi,
753 M. Kolb, K. Tetzlaff, S. Stowasser, C. Coeck, E. Clerisme-Beaty, B. Rosenstock, M.
754 Quaresma, T. Haeufel, R.-G. Goeldner, R. Schlenker-Herceg, K. K. Brown, INBUILD
755 Trial Investigators, Nintedanib in progressive fibrosing interstitial lung diseases. *N. Engl.*
756 *J. Med.* **381**, 1718–1727 (2019).

757 45. C. Grönberg, S. Rattik, C. Tran-Manh, X. Zhou, A. Rius Rigau, Y.-N. Li, A.-H. Györfi,
758 N. Dickel, M. Kunz, A. Kreuter, E.-A. Matei, H. Zhu, P. Skoog, D. Liberg, J. H. Distler,
759 T. Trinh-Minh, Combined inhibition of IL-1, IL-33 and IL-36 signalling by targeting
760 IL1RAP ameliorates skin and lung fibrosis in preclinical models of systemic sclerosis.
761 *Ann. Rheum. Dis.* **83**, 1156–1168 (2024).

762 46. F. van den Hoogen, D. Khanna, J. Fransen, S. R. Johnson, M. Baron, A. Tyndall, M.
763 Matucci-Cerinic, R. P. Naden, T. A. Medsger Jr, P. E. Carreira, G. Riemekasten, P. J.

764 Clements, C. P. Denton, O. Distler, Y. Allanore, D. E. Furst, A. Gabrielli, M. D. Mayes,
765 J. M. van Laar, J. R. Seibold, L. Czirjak, V. D. Steen, M. Inanc, O. Kowal-Bielecka, U.
766 Müller-Ladner, G. Valentini, D. J. Veale, M. C. Vonk, U. A. Walker, L. Chung, D. H.
767 Collier, M. E. Csuka, B. J. Fessler, S. Guiducci, A. Herrick, V. M. Hsu, S. Jimenez, B.
768 Kahaleh, P. A. Merkel, S. Sierakowski, R. M. Silver, R. W. Simms, J. Varga, J. E. Pope,
769 2013 classification criteria for systemic sclerosis: an American College of
770 Rheumatology/European League against Rheumatism collaborative initiative:
771 ACR/EULAR classification criteria for SSc. *Arthritis Rheum.* **65**, 2737–2747 (2013).

772 47. A. Chen, Y. Sun, Y. Lei, C. Li, S. Liao, J. Meng, Y. Bai, Z. Liu, Z. Liang, Z. Zhu, N.
773 Yuan, H. Yang, Z. Wu, F. Lin, K. Wang, M. Li, S. Zhang, M. Yang, T. Fei, Z. Zhuang,
774 Y. Huang, Y. Zhang, Y. Xu, L. Cui, R. Zhang, L. Han, X. Sun, B. Chen, W. Li, B. Huangfu,
775 K. Ma, J. Ma, Z. Li, Y. Lin, H. Wang, Y. Zhong, H. Zhang, Q. Yu, Y. Wang, X. Liu, J.
776 Peng, C. Liu, W. Chen, W. Pan, Y. An, S. Xia, Y. Lu, M. Wang, X. Song, S. Liu, Z. Wang,
777 C. Gong, X. Huang, Y. Yuan, Y. Zhao, Q. Chai, X. Tan, J. Liu, M. Zheng, S. Li, Y. Huang,
778 Y. Hong, Z. Huang, M. Li, M. Jin, Y. Li, H. Zhang, S. Sun, L. Gao, Y. Bai, M. Cheng, G.
779 Hu, S. Liu, B. Wang, B. Xiang, S. Li, H. Li, M. Chen, S. Wang, M. Li, W. Liu, X. Liu, Q.
780 Zhao, M. Lisby, J. Wang, J. Fang, Y. Lin, Q. Xie, Z. Liu, J. He, H. Xu, W. Huang, J.
781 Mulder, H. Yang, Y. Sun, M. Uhlen, M. Poo, J. Wang, J. Yao, W. Wei, Y. Li, Z. Shen, L.
782 Liu, Z. Liu, X. Xu, C. Li, Single-cell spatial transcriptome reveals cell-type organization
783 in the macaque cortex. *Cell* **186**, 3726–3743.e24 (2023).

784 48. F. A. Wolf, P. Angerer, F. J. Theis, SCANPY: large-scale single-cell gene expression data
785 analysis. *Genome Biol.* **19**, 15 (2018).

786 49. I. Korsunsky, N. Millard, J. Fan, K. Slowikowski, F. Zhang, K. Wei, Y. Baglaenko, M.
787 Brenner, P.-R. Loh, S. Raychaudhuri, Fast, sensitive and accurate integration of single-
788 cell data with Harmony. *Nat. Methods* **16**, 1289–1296 (2019).

789 50. V. Kleshchevnikov, A. Shmatko, E. Dann, A. Aivazidis, H. W. King, T. Li, R. Elmentaite,
790 A. Lomakin, V. Kedlian, A. Gayoso, M. S. Jain, J. S. Park, L. Ramona, E. Tuck, A.
791 Arutyunyan, R. Vento-Tormo, M. Gerstung, L. James, O. Stegle, O. A. Bayraktar,
792 Cell2location maps fine-grained cell types in spatial transcriptomics. *Nat. Biotechnol.* **40**,
793 661–671 (2022).

794 51. P. Badia-I-Mompel, J. Vélez Santiago, J. Braunger, C. Geiss, D. Dimitrov, S. Müller-Dott,

P. Taus, A. Dugourd, C. H. Holland, R. O. Ramirez Flores, J. Saez-Rodriguez, decoupleR: ensemble of computational methods to infer biological activities from omics data. *Bioinform Adv* **2**, vbac016 (2022).

52. V. A. Traag, L. Waltman, N. J. van Eck, From Louvain to Leiden: guaranteeing well-connected communities. *Sci. Rep.* **9**, 5233 (2019).

53. Y. Hao, T. Stuart, M. H. Kowalski, S. Choudhary, P. Hoffman, A. Hartman, A. Srivastava, G. Molla, S. Madad, C. Fernandez-Granda, R. Satija, Dictionary learning for integrative, multimodal and scalable single-cell analysis. *Nat. Biotechnol.*, doi: 10.1038/s41587-023-01767-y (2023).

54. J. M. Granja, M. R. Corces, S. E. Pierce, S. T. Bagdatli, H. Choudhry, H. Y. Chang, W. J. Greenleaf, ArchR is a scalable software package for integrative single-cell chromatin accessibility analysis. *Nat. Genet.* **53**, 403–411 (2021).

55. M. Liang, L. Wang, X. Tian, K. Wang, X. Zhu, L. Huang, Q. Li, W. Ye, C. Chen, H. Yang, W. Wu, X. Chen, X. Zhu, Y. Xue, W. Wan, Y. Wu, L. Lu, J. Wang, H. Zou, T. Ying, F. Zhou, Identification and validation of anti-protein arginine methyltransferase 5 (PRMT5) antibody as a novel biomarker for systemic sclerosis (SSc). *Ann. Rheum. Dis.* **83**, 1144–1155 (2024).

Acknowledgments:

Natural Science Foundation of China (NSFC) 82371818 (ML)

Joint Sino-German research project from NSFC and Deutsche Forschungsgemeinschaft (DFG, German Research Foundation) 82161138022 (JHWD and HZ)

Huashan Cultivation research 30302164001 (ML)

Huashan Innovation project 2024CX01 (ML)

Shanghai Oriental Youth Talent program DFYCQN07 (ML)

Rappaport MGH Research Scholar Award (LP)

Acknowledgments:

We would particularly like to acknowledge my colleagues, Division of Rheumatology of Huashan Hospital, Fudan University, for their wonderful collaboration and support. We are also deeply grateful to the patients who generously provided the samples used in this study.

Their contributions are invaluable to our research.

Author contributions:

Conceptualization: ML and ZL

Methodology: ZL, ML, ARR, WX, LH, XS, YNL, AEM, WY

Investigation: ZL, ML, ARR

Visualization: ZL, ML, ARR

Funding acquisition: ML, JHWD, LP and HZ

Project administration: ML

Supervision: ML, ZL, JHWD, RH

Writing – original draft: ML and ZL

Writing – review & editing: ZL, ARR, WX, LH, XS, YNL, AEM, WY, HZ, LP, JHWD, RH, ML

Competing interests: Although no disclosures directly relate to the present study, JHWD has consultancy relationships with Active Biotech, Anamar, ARXX, AstraZeneca, Bayer Pharma, Boehringer Ingelheim, Callidatas, Celgene, Galapagos, GSK, Inventiva, Janssen, Kyverna, Novartis, Pfizer, Quell Therapeutics and UCB, has received research funding from Anamar, ARXX, BMS, Bayer Pharma, Boehringer Ingelheim, Cantargia, Celgene, CSL Behring, Exo Therapeutics, Galapagos, GSK, Incyte, Inventiva, Kiniksa, Kyverna, Lassen Therapeutics, Mestag, Sanofi-Aventis, RedX, UCB and ZenasBio and is CEO of 4D Science and scientific lead of FibroCure. LP has financial interests in Edilytics, Inc., and SeQure Dx, Inc.

Data and materials availability: The spatial transcriptomics data presented in this study are available at the Zenodo data archive (https://zenodo.org/records/14577696). The scRNA-seq data for human skin were downloaded from GEO with the accession number GSE195452 (Gur2022) and GSE138669 (Tabib2021). A cross-tissue human fibroblast atlas was analyzed with the interface website http://pan-fib.cancer-pku.cn (Gao2024). The scRNA-seq data of full-thickness injuries in skin from reindeer was analyzed with the interface website www.biernaskielab.ca/reindeer_atlas (Sinha2022). The scRNA-seq data for mouse skin were downloaded from the Zenodo data archive (https://zenodo.org/records/7455989). The codes used in this study are available on Github: https://github.com/lzj1769/Spatial_SSc_project

Figures:

Fig. 1

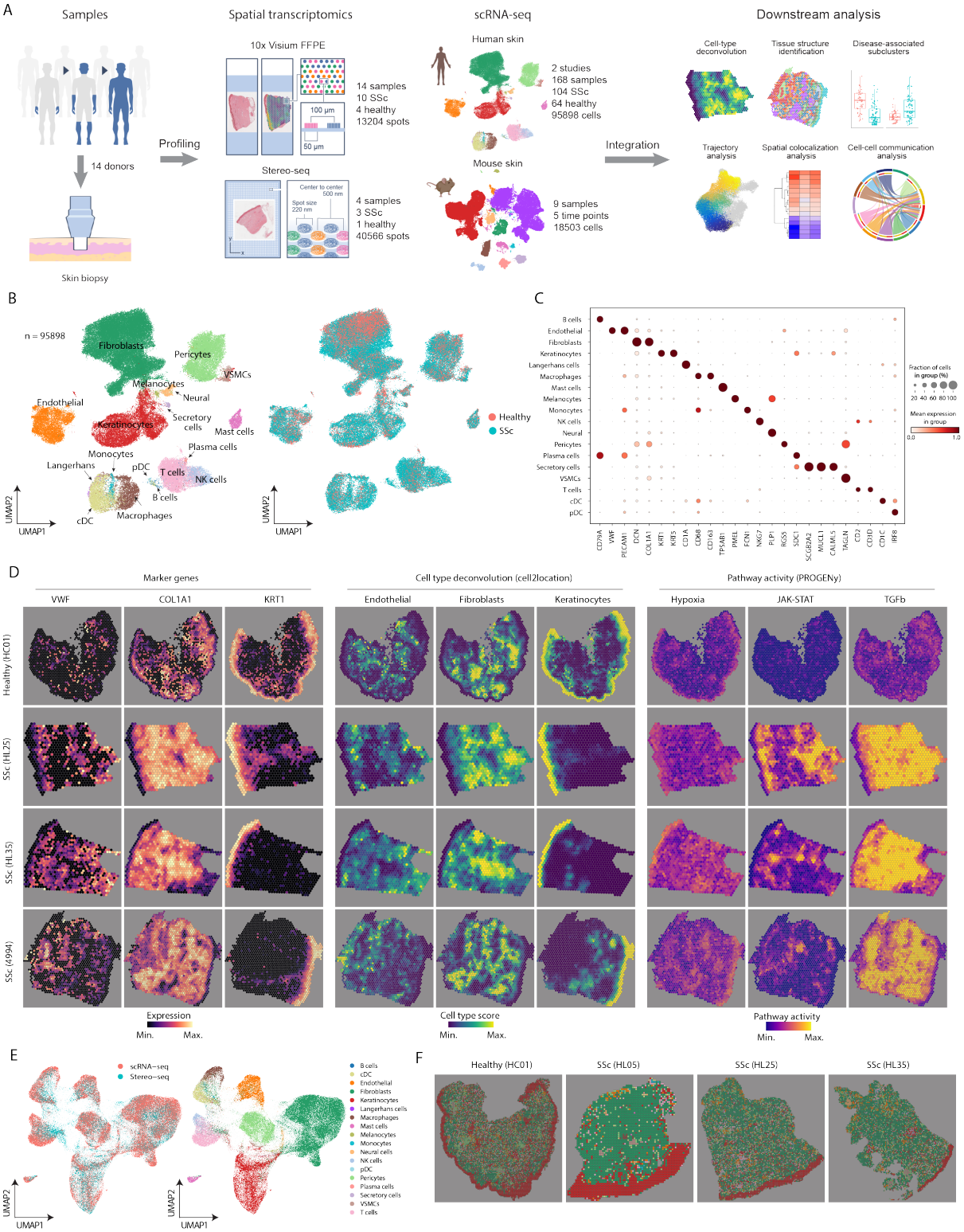

Fig. 1 Spatial profiling of human skin. (**A**), Overview of experimental design and analysis workflow. (**B**), UMAP showing integrated scRNA-seq datasets as colored by cell types (left)

and conditions (right). SSc skin n=104, Healthy skin n=64. (**C**), Dotplot showing gene expression for marker genes. The colors refer to the mean expression of the genes and the dot sizes represent the proportion of cells expressing the marker genes. (**D**), Visualization maps based on 10× Visium. SSc skin n=10, Healthy skin n=4. Left: *vWF*, *COL1A1*, and *KRT1* gene expressions in spatial transcriptomics data. Middle: representative cell types estimated by cell2location. Right: visualization of pathway activity in spatial space. (**E**), Integration of scRNA-seq and Stereo-seq data colored by protocols (left) and cell types (right). (**F**), Visualization of cell types in spatial space based on Stereo-seq data. SSc skin n=3, Healthy skin n=1. The experiments were performed on adjacent tissue sections to those used for 10× Visium.

Fig. 2

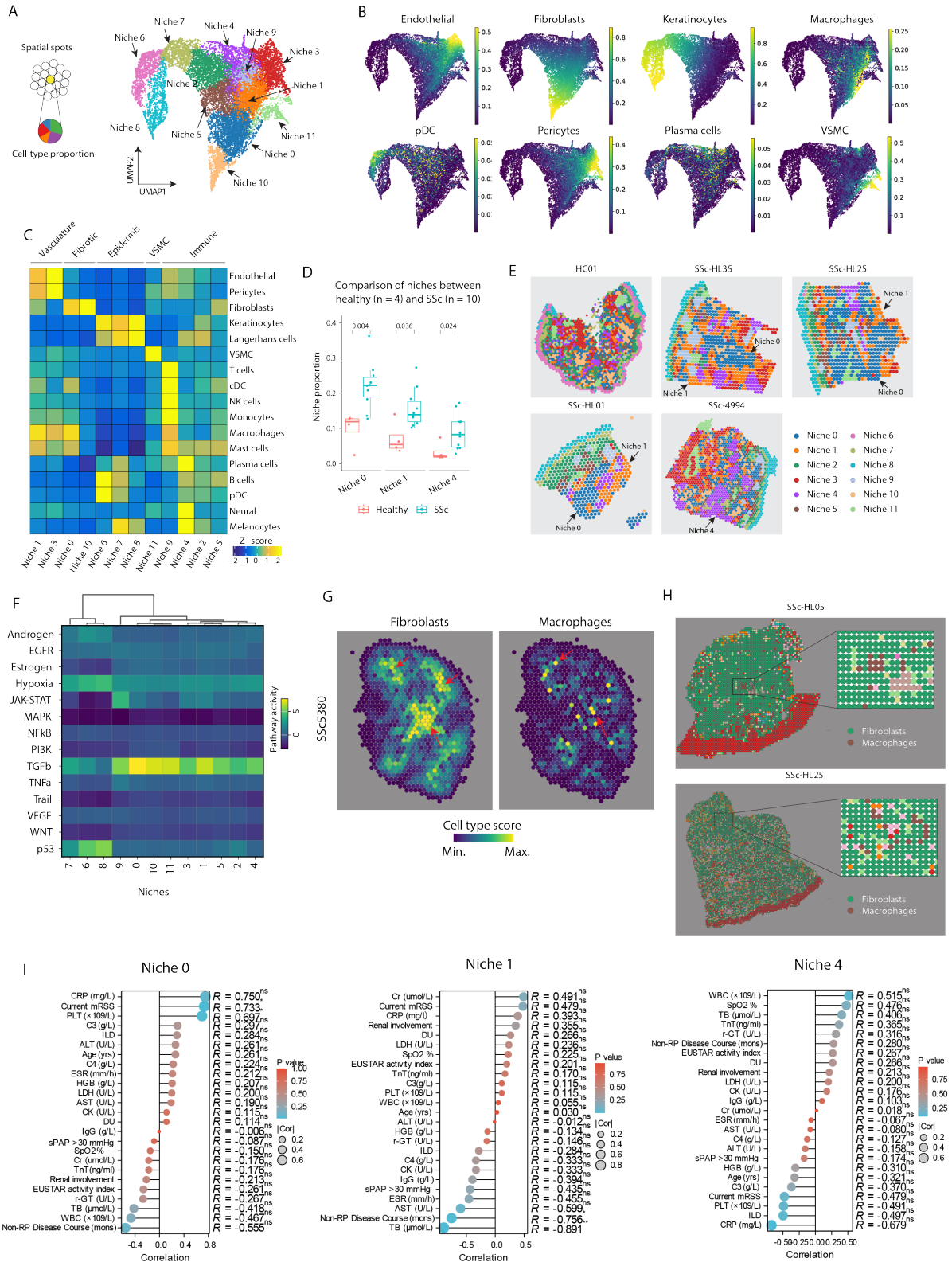

Fig. 2 Characterization of cell-type niches in SSc and healthy skin. (**A**), UMAP showing the integrated spatial data as colored by cell-type niches. (**B**), Visualization of cell type proportion in UMAP space. (**C**), Heatmap showing the enrichment of cell types in niches. Each column represents a niche, and each row represents a cell type. Colors refer to the z-score

905 transformed proportions of each cell type across different niches. (**D**), Boxplot comparing the
906 proportion of each niche between SSc and healthy skin samples. Each dot represents a sample.
907 *P*-values are calculated using the Wilcoxon rank-sum test (unpaired; two sides). (**E**),
908 Visualization of cell-type niches in spatial space for the healthy and SSc samples using 10x
909 Visium data. (**F**), Heatmap showing pathway activity for each niche. (**G**), Visualization of
910 fibroblasts and macrophages in spatial space using 10x Visium data. (**H**), Visualization of cell
911 types in spatial space using Stereo-seq data. (**I**), Correlations between the proportion of the
912 indicated niches with clinic statistics across all SSc subjects. Statistical significance was
913 determined by the Spearman test for a two-variable correlation. The correlation coefficient r is
914 indicated in figures (* $p < 0.05$).
915
916 **Abbreviations**: CRP (C-reactive protein), mRSS (Modified Rodnan Skin Score), PLT (platelet
917 count), C3 (complement component 3), ILD (interstitial lung disease), ALT (alanine
918 aminotransferase), C4 (complement component 4), ESR (erythrocyte sedimentation rate), HGB
919 (hemoglobin), LDH (lactate dehydrogenase), AST (aspartate aminotransferase), CK (creatine
920 kinase), DU (digital ulcer), IgG (immunoglobulin G), sPAP (systolic pulmonary arterial
921 pressure), SpO2 (oxygen saturation), Cr (creatinine), TnT (troponin T), EUSTAR activity
922 index (European Scleroderma Trials and Research Group activity index), r-GT (gamma-
923 glutamyl transferase), TB (total bilirubin), WBC (white blood cell count), and Non-RP Disease
924 Course (non-raynaud's phenomenon disease course).
925
926
927
928
929
930
931
932
933
934
935
936
937

Fig. 3

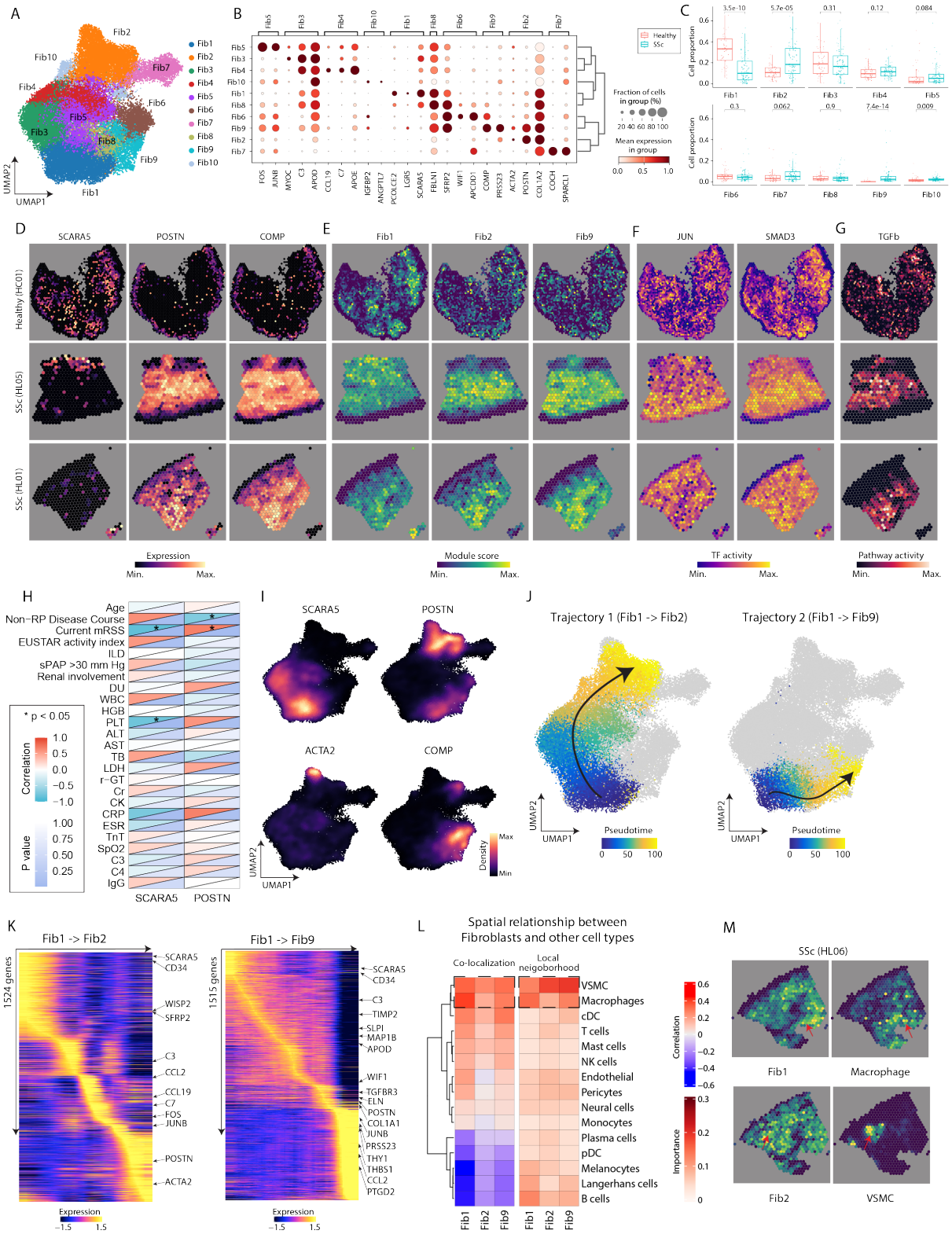

Fig. 3 Characterization of fibroblast sub-populations. (**A**), UMAP showing sub-populations of fibroblasts based on scRNA-seq data. (**B**), Dot plot showing the marker genes of each subset. (**C**), Bar graph comparing the proportion of each fibroblast subset between healthy and SSc samples. Each dot represents a sample. *p*-values are calculated using the Wilcoxon rank-sum

test (unpaired; two sides). (**D**), Visualization of *SCARA5, POSTN*, and *COMP* expression in spatial space. (**E**), Visualization of module score of Fib1, Fib2, and Fib9 in spatial space. (**F**), Visualization of TF activity of JUN and SMAD3 in spatial space. (**G**), Visualization of TGF-β pathway activity in spatial space. (**H**), Heatmap showing correlations between expressions of *SCARA5* and *POSTN* and different clinical outcomes of SSc. The colors in the upper left square represent Spearman's r value, while those in the lower right square represent p values (* $p < 0.05$). (**I**), Expression of *SCARA5, POSTN, ACTA2*, and *COMP* overlaying with UMAP. (**J**), UMAP showing the differentiation trajectory from Fib1 to Fib2 (left), and Fib1 to Fib9 (right). Colors refer to pseudotime points. (**K**), Heatmap showing the gene expression dynamics during the trajectory from Fib1 to Fib2 (left), and Fib1 to Fib9 (right). (**L**), co-localization between major cell types and fibroblast sub-clusters (Fib1, Fib2 and Fib9) as measured within the same spot (left) and neighboring spots (right). (**M**), Visualization of the abundance of macrophages and VSMCs and the state scores of Fib1 and Fib2 in a representative SSc skin sample.

Fig. 4

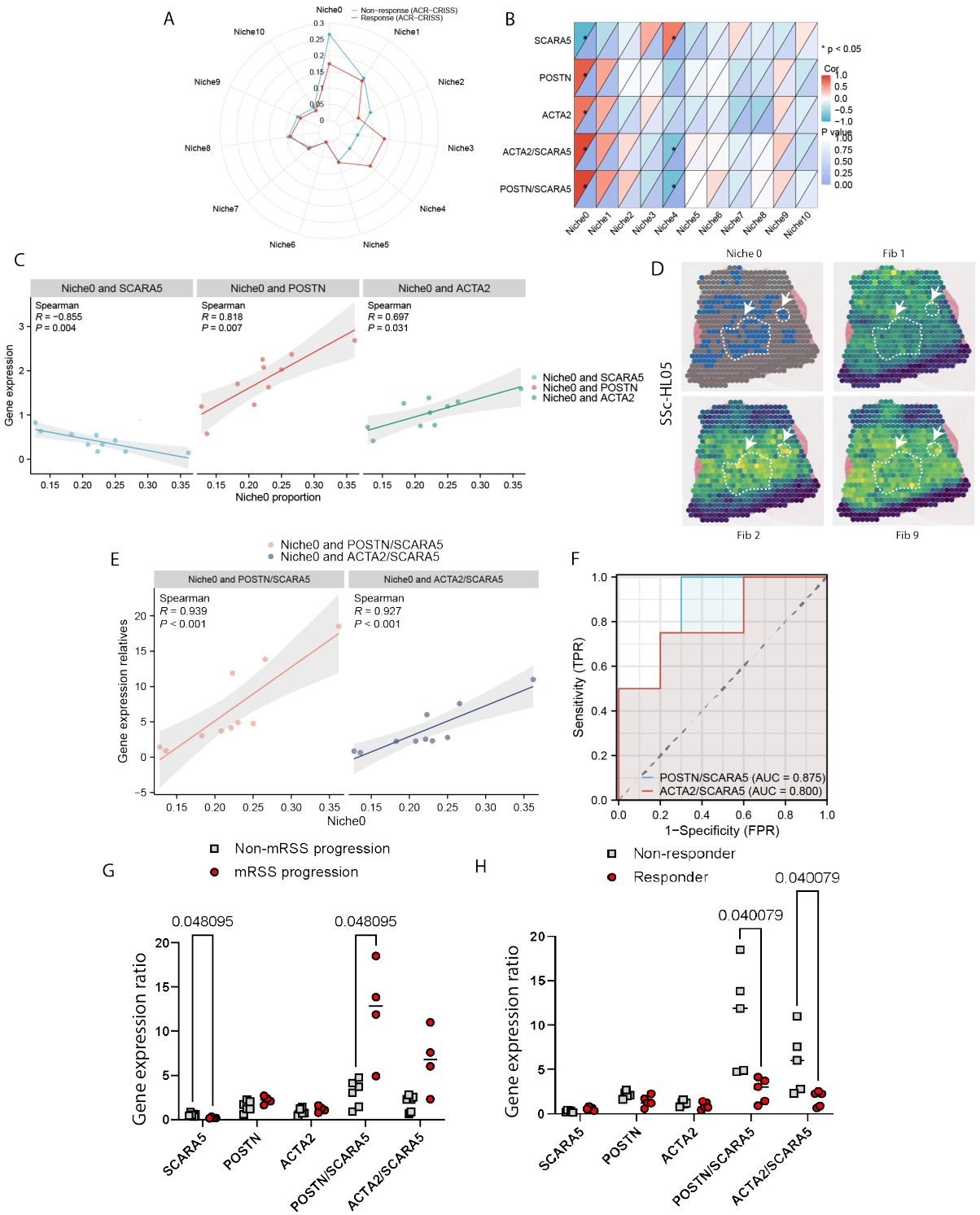

Fig. 4 Correlations of the cellular phenotype with clinical outcomes. (**A**), A radar plot displaying the proportions of the identified niches in SSc patients, distinguishing between those who were responsive to the standard treatment of Mycophenolate Mofetil (MMF) and those who were not. (**B**), Heatmap showing correlations between the proportion of each niche and the pseudo-bulk gene expression, along with the ratios of *POSTN/SCARA5* and

983 *ACTA2/SCARA5*. The colors in the upper left square represent Spearman's r value, while those
984 in the lower right square represent p values (* $p < 0.05$). (**C**), Correlations between the
985 proportion of niche 0, which was predominantly composed of fibroblasts and macrophages,
986 and the gene expressions of *SCARA5, POSTN, ACTA2*, along with their ratios. Correlation data
987 were analyzed using non-parametric Spearman tests. Each data point represents one SSc
988 sample, and the confidence interval (CI) is indicated by grey shadows. (**D**), Visualization of
989 the abundance of niche 0 and the state scores of Fib1, Fib2 and Fib9 in a representative SSc
990 skin sample. (**E**), Receiver operating characteristic (ROC) curve showing the discrimination of
991 SSc patients from healthy controls based on the gene expression ratios of *POSTN/SCARA5* and
992 *ACTA2/SCARA5*, respectively. The area under the curve (AUC) values are indicated in graphs.
993 (**F**), The gene expressions of *SCARA5, POSTN, ACTA2*, along with their ratios, comparing the
994 SSc patients who experienced skin fibrosis progression or not. (**G**), The gene expression of
995 *SCARA5, POSTN, ACTA2*, along with their ratios, comparing the SSc patients who were
996 responsive to the standard treatment of MMF or not, evaluated at a 52-week follow-up. Two-
997 sided Wilcoxon rank sum tests were conducted to compare the differences between the two
998 groups.
999
1000
1001
1002
1003
1004
1005
1006
1007
1008
1009
1010
1011
1012
1013
1014
1015
1016

1017 **Fig. 5**

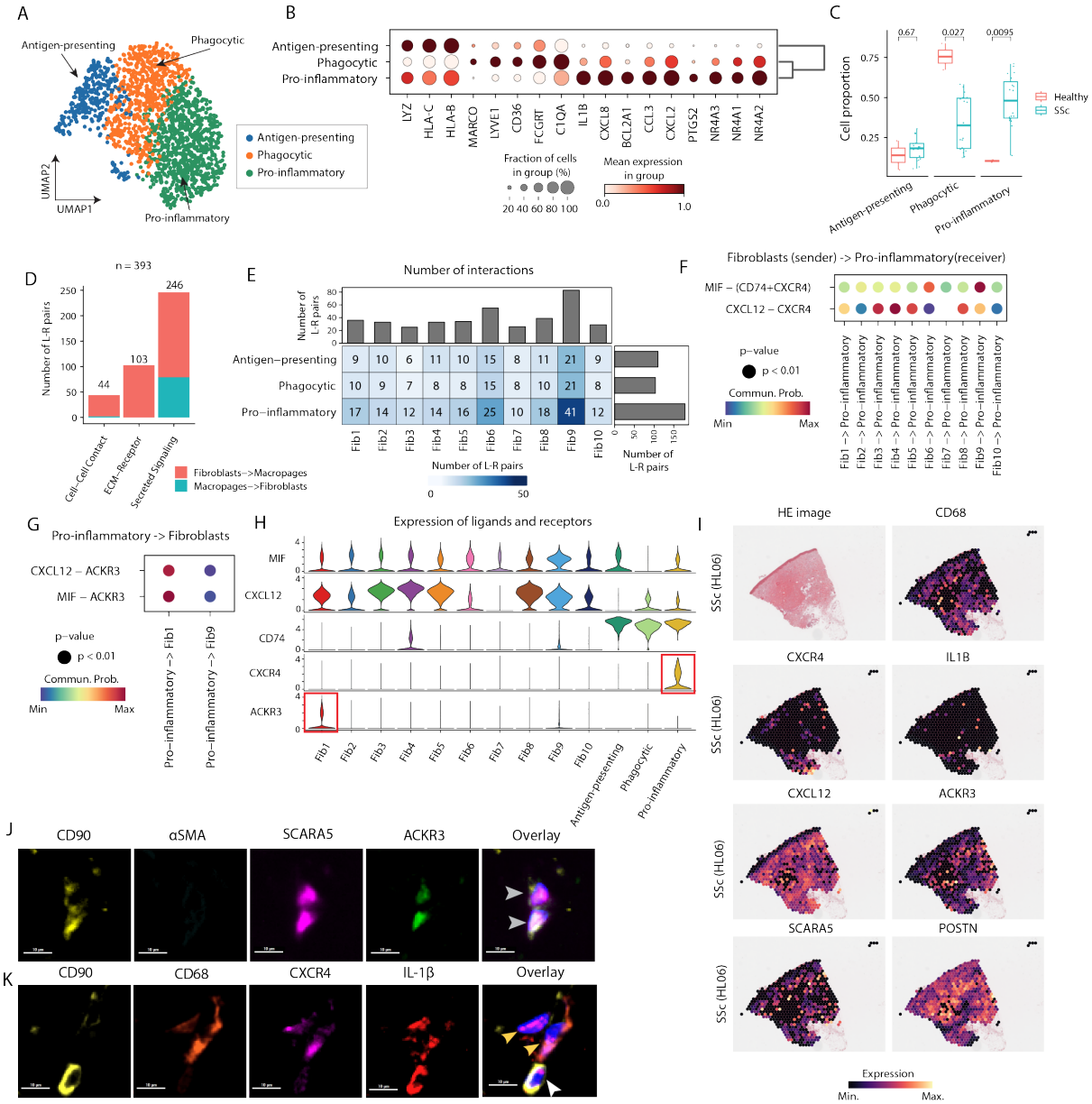

1018

1019 **Fig. 5 Characterization of macrophage sub-clusters.** (**A**), UMAP showing sub-clusters of
1020 macrophages based on scRNA-seq data. (**B**), Dotplot showing the marker genes for each sub-
1021 cluster. (**C**), Boxplot comparing the proportion of each sub-cluster between healthy and SSc
1022 samples. Each dot represents one sample. P-values are calculated using the Wilcoxon rank-sum
1023 test (unpaired; two sides). (**D-E**), Number of significant L-R pairs between the fibroblasts and
1024 macrophages. (**F**), Heatmap showing significant ligand-receptor pairs between fibroblast
1025 subsets and proinflammatory macrophages, with fibroblast serving as signaling senders and
1026 macrophage as receivers. The colors refer to the communication probability and the sizes
1027 represent p-values. (**G**), Heatmap showing significant ligand-receptor pairs between

1028 proinflammatory macrophages and fibroblast subsets (Fib1, Fib9), as macrophage serving as
1029 signaling senders and fibroblast as receivers. (**H**), Violin plot showing the expression of ligands
1030 and receptors in scRNA-seq. (**I**), Expression of ligands and receptors in spatial space. (**J**),
1031 Representative images of TSA (Tyramide Signal Amplification) staining on the expression of
1032 ACKR3 in SCARA5^{+} fibroblast which are labeled with CD90 (indicated by grey arrows). (**K**),
1033 Representative images of TSA staining on the co-occurrence of fibroblasts (marked by CD90
1034 and indicated by a white arrow) with IL-1β^{+}macrophages, which are also positive for CXCR4
1035 (indicated by yellow arrows). The staining in J and K were performed on adjacent tissue
1036 sections to those used for 10× Visium. Horizontal scale bars represent 10 μm.

1037

1038 **Fig. 6**

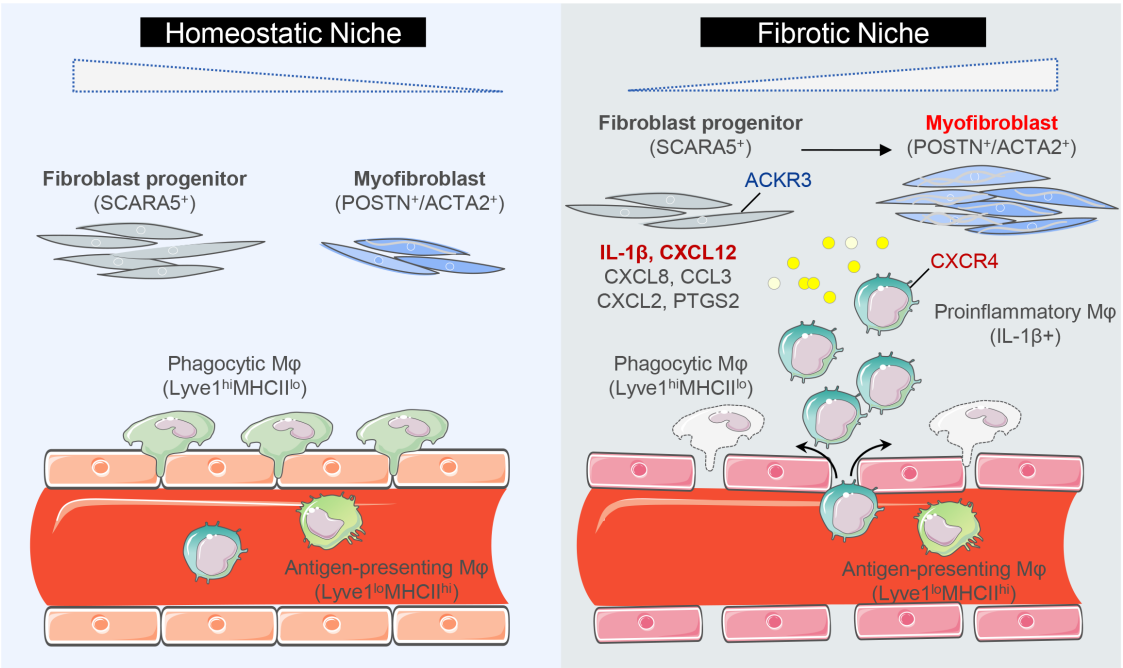

1039

1040 **Fig. 6 A Data-Driven Model of SSc.** Schematic summary illustrates the proposed cellular
1041 interplay in SSc skin, which leads to a shift from tissue homeostasis to a fibrogenic environment.
1042 The illustration was created by using images from Servier Medical Art
1043 (http://smart.servier.com/), licensed under CC BY 3.0
1044 (https://creativecommons.org/licenses/by/3.0/).

Mapping spatially-resolved transcriptomes in systemic sclerosis

Supplementary Materials and Methods

Human skin biopsy collection and processing

Skin biopsies from 14 SSc subjects and 4 age- and gender-matched healthy controls were obtained and proceeded for spatial transcriptomics using the 10x Visium platform. All skin biopsies of SSc patients were taken on the forearm 15 ± 2 cm proximal from the styloid process of the ulna using disposable biopsy punches (pfm medical, #48301, Gifu, Japan). The epidemiological and clinical features of the SSc patients are presented in table S1. After excluding 2 low-quality SSc samples (**fig S1**), we finally included 14 skin biopsies in total, from10 SSc patients and 4 healthy controls. SSc was diagnosed according to the American College of Rheumatology (ACR) /European Alliance of Associations for Rheumatology (EULAR) 2013 criteria(*46*). In particular, we enrolled SSc patients who had diffused cutaneous involvement and had experienced their initial non-Raynaud's phenomenon symptoms for less than three years. Among the SSc patients, 40% were female and 60% were male. The median age at biopsy of SSc patients was 56.0 years (range 27-73). The median disease duration from the first non-RP symptoms was 8 months (range 4-48). The median mRSS was 21 (range 8-41). 40% of SSc patients suffered from interstitial lung disease (ILD). All the SSc patients included in our study were treatment-naive and received the standard treatment of MMF for consecutive 52 weeks following skin biopsy. The responsiveness was defined according to the criteria of the revised ACR-CRISS (American College of Rheumatology Composite Response Index in Systemic Sclerosis), which is the improvement in ≥ 3 of 5 core clinical measurements with Minimal Clinically Important Difference (MCID) of 25% for modified Rodnan skin score (mRSS), 5% for percent predicted forced vital capacity (FVC%), 20% for health assessment questionnaire-disability index (HAQ-DI), 20% for patient (PGA) and clinician (CGA) global assessments(29). SSc patients with progression of skin fibrosis, which is defined as increase in modified Rodnan skin score (mRSS) ≥ 25% from baseline in the 52-week follow-up visit after baseline. All human studies were approved by the ethical committees of Huashan Hospital of Fudan University. All patients and controls signed a consent form approved by the local institutional review board after informed consent.

Spatially profiling human skin with 10x Visium

Formalin-fixed paraffin-embedded (FFPE) skin blocks from a total of 18 subjects were sectioned at 5 um thickness. These sections were transferred to match the 6.5mm^2 oligo-barcoded capture areas on the 10x Visium platform (FFPE v2) according to the manufacturer's protocol. Prior to this, archived tissues from paraffin-embedded blocks were tested for RNA quality control (DV200 > 30%), before being mounted on the 10× CytAssist (6.5 mm × 6.5 mm) for library preparation and sequencing (~50,000 reads/spot). Hematoxylin and eosin (H&E) staining was conducted for morphological assessment. The Visium Human Transcriptome Probe Set v2.0 was applied. The final library pool was sequenced on the Illumina Novaseq 6000 instrument using 150-base-pair paired-end reads.

Spatially profiling human skin with Stereo-seq

To achieve an enhanced resolution and whole transcriptome in-situ analysis of skin samples, we employed Stereo-seq technology according to the previous protocols(*16*, *47*), which enables the spatial detection of transcriptome-wide gene expression at a resolution of 0.5 um. Briefly, 5-um FFPE skin sections from 3 SSc patients and 1 healthy control, which are overlapping with the ones who underwent the examination of 10x Visium, were subjected to adhere to the Stereo-seq chips which have DNA nanoball (DNB) bins with 220 nm diameter and a center-to-center distance of 500 nm. After methanol fixation, the formal sections were preceded with ssDNA staining and the adjacent sections with H&E staining for morphological assessment. Next, permeabilization of the tissue was performed to release mRNA. cDNA products are synthesized by reversed transcription. After amplification, DNBs were then generated via rolling cycle amplification (RCA) and loaded onto the patterned chips (65mm×65mm). Next, to determine the distinct DNB-CID sequences at each spatial location, paired-end sequencing was performed on a DNBSEQ-T7 sequencer (MGI Research, Shenzhen, China) with a PE75 sequencing strategy.

Processing 10x Visium and Stereo-seq data

For 10x Visium data, we used SpaceRanger software (v2.0.0) to pre-process the raw sequencing data based on the reference genome hg38. For each sample, we filtered the spots by number of detected genes (< 100). For Stereo-seq data, we leveraged nucleic acid staining from the same section to segment cells by projecting the staining image to the Stereo-seq chips. The watershed algorithm was applied to the staining image for single cell segmentations. For each of the segmented cells, UMI from all DNB within the corresponding segmentation were aggregated per-gene and then summed to generate a cell by gene matrix for downstream

analysis. To overcome the low RNA capture efficiencies on single DNB spots at a resolution of 500 nm, the raw spatial expression matrix was convoluted into larger pseudo-spots with a 50×50 window size (bin50 for short), or more precisely, as 25 μm squares. We then filtered the spots by number of detected genes (< 50) and mitochondrial genes (> 10%).

Analysis of publicly available scRNA-seq data

To build an atlas of human skin cells, we downloaded scRNA-seq data from Gene Expression Omnibus (GEO) with accession numbers GSE195452 (denoted by Gur2022)(*10*) and GSE138669 (denoted by Tabib2021)(*9*). For the Gur2022 dataset, we only kept the cells from the skin. We further filtered the cells by number of UMIs (< 500), number of detected genes (< 300 or > 5000), and mitochondrial genes (> 30%). We also filtered the genes by the number of cells (n = 100). We re-annotated the cells by merging the 49 original labels to 16 major cell types as follows: Fibroblast (Fibro_ATAC2, Fibro_Bad, Fibro_COCH, Fibro_COMP, Fibro_IGFBP2, Fibro_LGR5, Fibro_MYOC1, Fibro_MYOC2, Fibro_POSTN, Fibro_PTGDS, Fibro_POSTN_PTGDS), T cells (sT_Effector, T_Effector, T_GD, T_Naive, sTreg_CXCR4, sTreg, Treg, sT), NK cells (NK, NK_XCL1, NK_XCL1_CXCR4), cDC (DC, DC_CCL22, DC_CXCL10, DC_XCR1), Macrophages (Mf, Mf_TREM2), Monocytes (Mo_CD16, M_CD16_IL1B, M_IL1B, Mo), Mast cells (bMast_CLC, Mast), B cells (B, B_CXCR4), Pericytes (Peri_RGS5, Peri_TGFBI), Endothelial cells (Vascular_ACKR1, Vascular_RBP7), Keratinocytes (KRT1_KRT10, KRT14_ACTA2, KRT14_S100A2_GJA1). For the Tabib2021 dataset, we filtered the cells by UMIs (<500), number of detected genes (<300 and >5000), and mitochondrial gene expression (>5%). Since the original annotation was unavailable, we clustered and re-annotated the cells. This recovered 13 major cell types, among which 10 cell types were also identified by the Gur2022 dataset. To integrate these two datasets, we merged the count matrices and normalized the data using Scanpy(*48*). Next, we used the Harmony algorithm(*49*) to correct the batch effects between the datasets and visualize the integrated cells by UMAP.

Cell type deconvolution of 10x Visium data

We used cell2location(*50*) and the above scRNA-seq data as a reference to estimate cell type composition for each spot in the spatial transcriptomics samples. Specifically, we first identified the signatures of each cell type using the scRNA-seq data based on a Negative binomial regression model after accounting for the batch effects from different datasets. Next,

we removed all mitochondrial genes, subsetting the reference data and spatial data using the identified signatures. We ran the function Cell2location (N_cells_per_location=5; detection_alpha=20) to estimate posterior distributions of cell abundance. We normalized the estimated cell type composition for each spot to [0, 1], which was used for visualization and downstream analysis.

Inference of pathway activity for 10x Visium data

We used decoupeR(*51*) (v1.8.0) to infer the pathway and transcription factor activity. Specifically, for each sample, we normalized the expression counts matrix and identified highly variable genes using Scanpy(*48*). Next, we obtained a collection of pathways and their target genes using the function get_progeny (organism='human', top=500). The pathway enrichment scores were inferred using the multivariate linear model by running the function run_mlm.

Integration of scRNA-seq and Stereo-seq data

We used Seurat (v5.1.0) to integrate the scRNA-seq and Stereo-seq data. Specifically, we merged the Stereo-seq samples and then identified a set of anchors between these two datasets using the function FindTransferAnchors (reduction = "cca") based on the shared genes (n = 11110). Next, we transferred the cell type labels from scRNA-seq to Stereo-seq data using the function TransferData (weight.reduction = "cca", dims = 1:30). To integrate the data in a common embedding space, we also transferred the batch-corrected PCA components (n = 30) from scRNA-seq to Stereo-seq data with the function TransferData. Next, we run the function RunUMAP to generate a co-embedding space to visualize integrated scRNA-seq and Stereo-seq data.

Identification of cell-type composition niches in 10x Visium data

We combined the cell type proportions estimated by cell2location from all samples to. Next, we ran the function neighbors (n_neighbors=30) to create a neighborhood graph of all spatial spots based on the cell type proportions. An UMAP embedding was generated using the function umap with default settings in Scanpy. We clustered the spots with the function leiden (resolution = 0.5), identifying 12 niches. To annotate the niches, we computed the average proportion for each cell type within each niche. We next normalized the values by z-score transformation and clustered the niches using hierarchical approach.

133

134 **Sub-clustering of fibroblasts**

135 We subsetted the fibroblasts and removed the samples with less than 100 cells to allow for
136 robust data integration. Next, we clustered the cells with the Leiden algorithm(*52*) (resolution
137 =1) based on the harmonized principal components. We removed one population with high
138 mitochondrial genes, resulting in a total of ten clusters identified. The marker genes for each
139 cluster were identified using the function rank_genes_groups (method='wilcoxon') from
140 Scanpy. To map these sub-clusters to spatial space, we selected the top 100 markers for each
141 cluster and then computed module scores using the function AddModuleScore from Seurat(*53*).

142

143 **Analysis of scRNA-seq data from mouse skin**

144 We downloaded scRNA-seq data from the Zenodo data archive
145 (https://zenodo.org/records/7455989). Cells were filtered by the number of UMIs (< 2000 or >
146 40000), number of detected genes (< 200 or > 6000) and fraction of mitochondrial genes (>
147 5%), retaining 18503 cells. Genes were filtered by the number of cells (< 50). Next, we
148 normalized the count matrix using the functions normalize_total and log1p from Scanpy.
149 Highly variable genes were selected by the function highly_variable_genes. We clustered the
150 cells with the Leiden algorithm (resolution = 0.5) based on the 30 principal components and
151 identified 25 populations which were further grouped into 14 cell types based on their canonical
152 markers. We next subsetted all fibroblasts and clustered the cells using the Leiden algorithm
153 (resolution=0.5), obtaining 10 sub-clusters. We noticed one cluster showing a low number of
154 UMIs and detected genes, presumably corresponding to low-quality cells. We therefore
155 removed this cluster and rename the remaining clusters as Fib1-9.

156

157 **Analysis of scRNA-seq data from reindeer**

158 The scRNA-seq data of full-thickness injuries in skin from reindeer was analyzed with the
159 interface website (www.biernaskielab.ca/reindeer_atlas)(*7*).

160

161 **Trajectory analysis of fibroblasts**

162 We used ArchR(*54*) to perform trajectory analysis. Specifically, we inferred two pseudo-time
163 trajectories using the function AddTrajectory to characterize the differentiation processed from
164 Fib1 to Fib2 (denoted by trajectory 1), and from Fib1 to Fib9 (denoted trajectory 2) based on
165 the principal components (n = 30). The trajectory 1 involved six subsets (Fib1, Fib3, Fib5, Fib4,

Fib10, and Fib2), and the trajectory 2 included only Fib1 and Fib9. The trajectories were visualized by the function TrajectoryPlot. To identify associated genes for each trajectory, we obtained the expression matrix along the trajectory using the function GetTrajectory (smoothWindow = 11). Next, we visualized the dynamics of gene expression with the function plotTrajectoryHeatmap and selected the top 10% highly variable genes across the trajectory.

Spatial relationship analysis between fibroblast subsets and other cell types

We used two approaches to infer spatial relationships between the subsets of fibroblasts and other major cell types. The first approach was based on Spearman correlation between the module score of each subset and the proportion of each major cell type across all spatial spots. This was performed for each 10x Visium sample independently, and results were averaged across all samples. The second approach was based on Misty. Specifically, we usd Misty to build a predictive model using the cell type proportions as features and module scores as target. This allows us to learn the spatial interactions between spots.

Sub-clustering of macrophages

We subsetted all macrophages from the integrated scRNA-seq atlas and removed samples with less than 50 cells. Next, clustered the cells using the Leiden algorithm(*52*) (resolution = 0.3) based on the harmonized principal components, identifying three sub-clusters. The marker genes for each cluster were identified using the function rank_genes_groups (method='wilcoxon') from Scanpy. To map these sub-clusters to spatial space, we selected the top 100 markers for each cluster and then computed module scores using the function AddModuleScore from Seurat(*53*).

Cell-cell communication analysis between fibroblasts and macrophages

We merged the fibroblast and macrophage subclusters to create a Seurat object. Next, we normalized the count matrix using the function NormalizeData from Seurat and identified highly variable genes using the function FindVariableFeatures. We created a CellChat object and grouped the cells based on the sub-clustering results as described above. We selected the database CellChatDB.human and excluded ligand-receptor pairs from non-protein signaling. The cell-cell communication network was inferred using the function computeCommunProb (type = "triMean") and was filtered using the function filterCommunication (min.cells = 10).

198

199 **Imaging mass cytometry (IMC)**

200 We performed data mining using our published IMC dataset(*15*), which included FFPE skin
201 biopsy sections from 19 SSc patients and 14 matched controls. The IMC panel included up to
202 38 lanthanide labeled antibodies as well as Iridium 193 and 191 isotopes, which were designed
203 to target epitopes specific for different subsets of endothelial cells, endothelial precursor cells,
204 immune cells and mesenchymal cells, as well as structural markers used for tissue segmentation.
205 Data acquisition was performed on a Helios time-of-flight mass cytometer coupled to a
206 Hyperion Imaging System (Standard Biotools). After single-cell segmentation and data
207 transformation and normalization, we obtained the single-cell dataset with spatial information
208 alongside. We then proceeded with dimensionality reduction, unsupervised clustering, and
209 subsequent cell type annotation. To investigate the local microenvironment of individual
210 fibroblast subpopulations, we identified cellular neighborhoods (CNs) by k-means clustering
211 on the composition of neighboring cells as described(*14*).

212

213 **Tyramide signal amplification (TSA)**

214 FFPE skin tissue sections obtained from 4 SSc patients and 4 control donors were stained using
215 a TSA system as previously described(*15*, *55*). Briefly, the sections were proceeded with
216 dewaxing, rehydration, and antigen retrieval with Tris-EDTA(pH 9.0) for 15 minutes.
217 Endogenous peroxidase activity was neutralized with 3% H_2O_2 for 10 minutes, followed by a
218 30-minute blocking step with antibody diluent/block buffer (ARD1001EA, AKOYA). Next,
219 sections were incubated for 90 min at room temperature with the following primary antibodies
220 of the indicated dilutions: SCARA5 (ab118894, 1:200, Abcam), CD90 (ab226123, 1:200,
221 Abcam), α-SMA (#19245, 1:200, Cell signaling), CD68 (ab192847, 1:200, Abcam), IL-1β
222 (ab283818, 1:200, Abcam), CXCR4 (ab181020, 1:200, Abcam) and ACKR3 (20423-1-AP,
223 1:200, Proteintech). After multiple rounds of signal amplification with Opal fluorophores and
224 subsequent antibody stripping, sections were stained with DAPI. Slides were scanned using a
225 PhenoImager Fusion scanner (Akoya Biosciences) to distinguish the spectra of the different
226 fluorescence channels. All images were captured and presented using the same equipment
227 setting. Merging channels was conducted using ImageJ / Fiji software (Release 2.16.0,
228 https://fiji.sc).

229

230

Statistics

Quantitative data are shown either as violin plots, bar graphs or scatter plots. Data in bar graphs are presented as median ± interquartile range (IQR) with individual data points plotted as dots. Statistical significance was calculated using R (4.4.2). Further statistical analysis on clinical correlation was also performed using GraphPad prism 8 version 8.3.0. We used nonparametric tests in this study. Two-sided Wilcoxon rank sum tests were used to perform two-group comparisons in Fig. 2D, Fig. 3C, Fig. 4G, Fig. 4H, Fig. 5C, and figs. 5 (C and D). Non-parametric Spearman correlation was used to assess relationships between continuous variables in Fig. 2I, Fig. 3H, Figs. 4 (C and E), and figs. S5 (C and D). P-values < 0.05 were considered statistically significant.

SUPPLEMENTAL FIGURES

Fig. S1

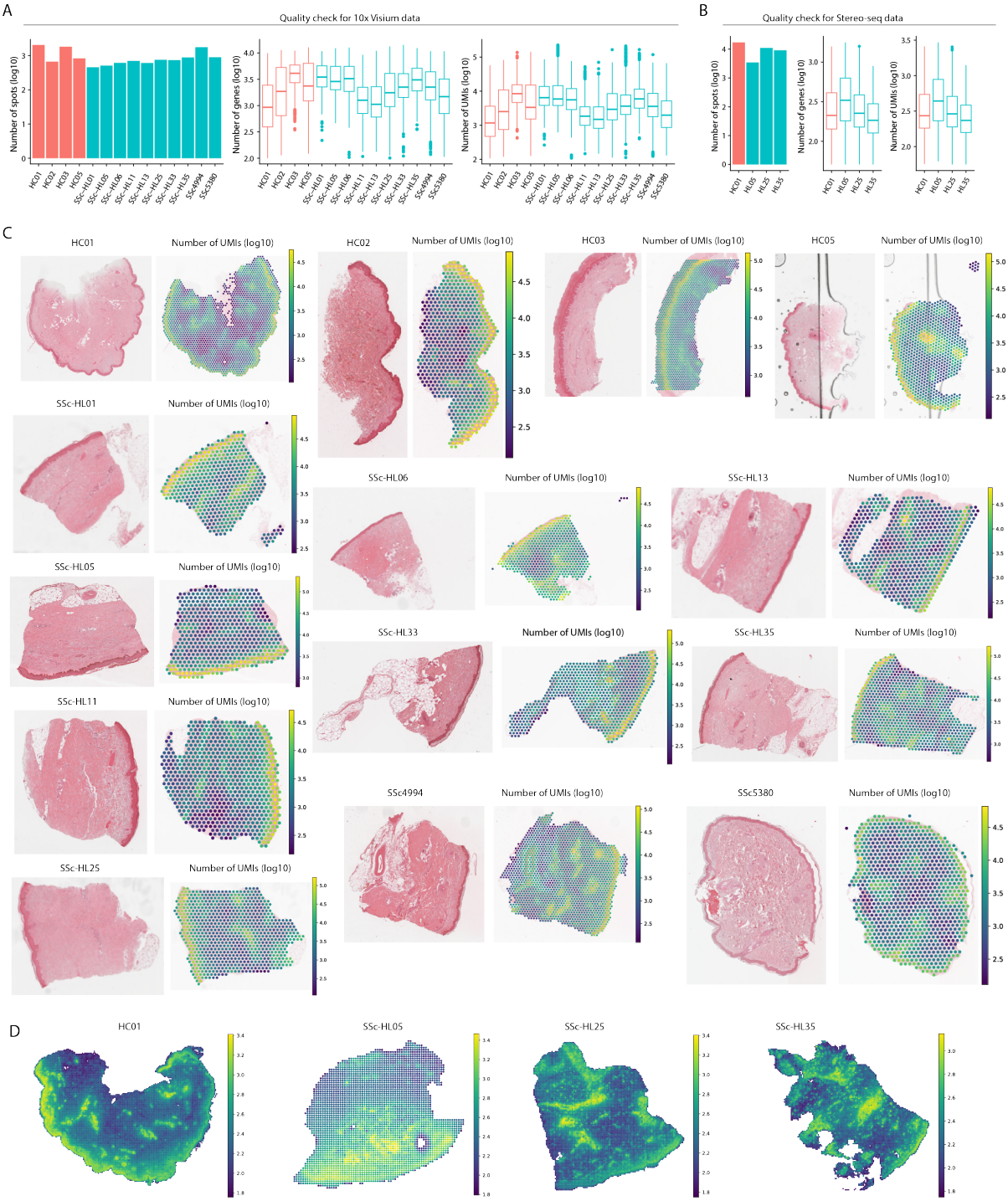

Fig. S1 Quality check of spatial transcriptomics data. (**A**), Left: number of detected spots per sample in 10x Visium data. Middle: number of genes per spot in each sample. Right: number of UMIs in each sample. (**B**), Left: number of detected spots per sample in Stereo-seq. Middle: number of genes per sample. Right: number of UMIs in each sample. (**C**), Visualization of H&E image and number of UMIs in spatial space for 10x Visium data. (**D**),

Visualization of number of UMIs in spatial space for Stereo-seq data.

Fig. S2

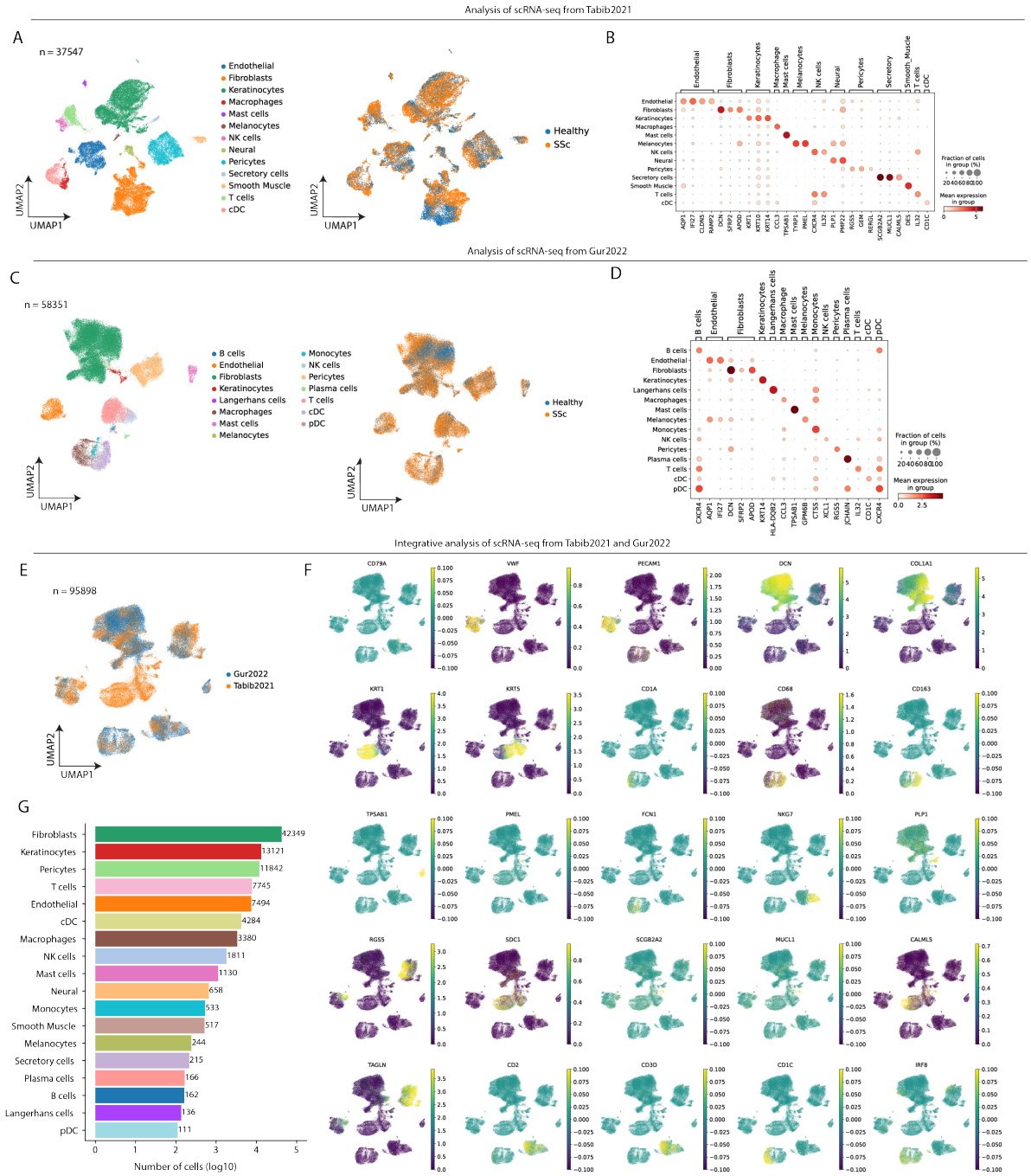

Fig. S2 Analysis of publicly available scRNA-seq data. (**A**), UMAP showing scRNA-seq from the Tabib2021 dataset as colored by cell types and conditions. Heatmap showing cell-type-specific marker genes. (**B**), UMAP showing scRNA-seq as colored by cell types and conditions. (**C**), Same as A for the Gur2022 dataset. (**D**), Same as B for the Gur2022 dataset. (**E**), UMAP showing the integrated scRNA-seq data colored by different datasets. (**F**), Visualization of cell-type-specific marker genes. (**G**), Barplot showing number of cells for each

cell type.

Fig. S3

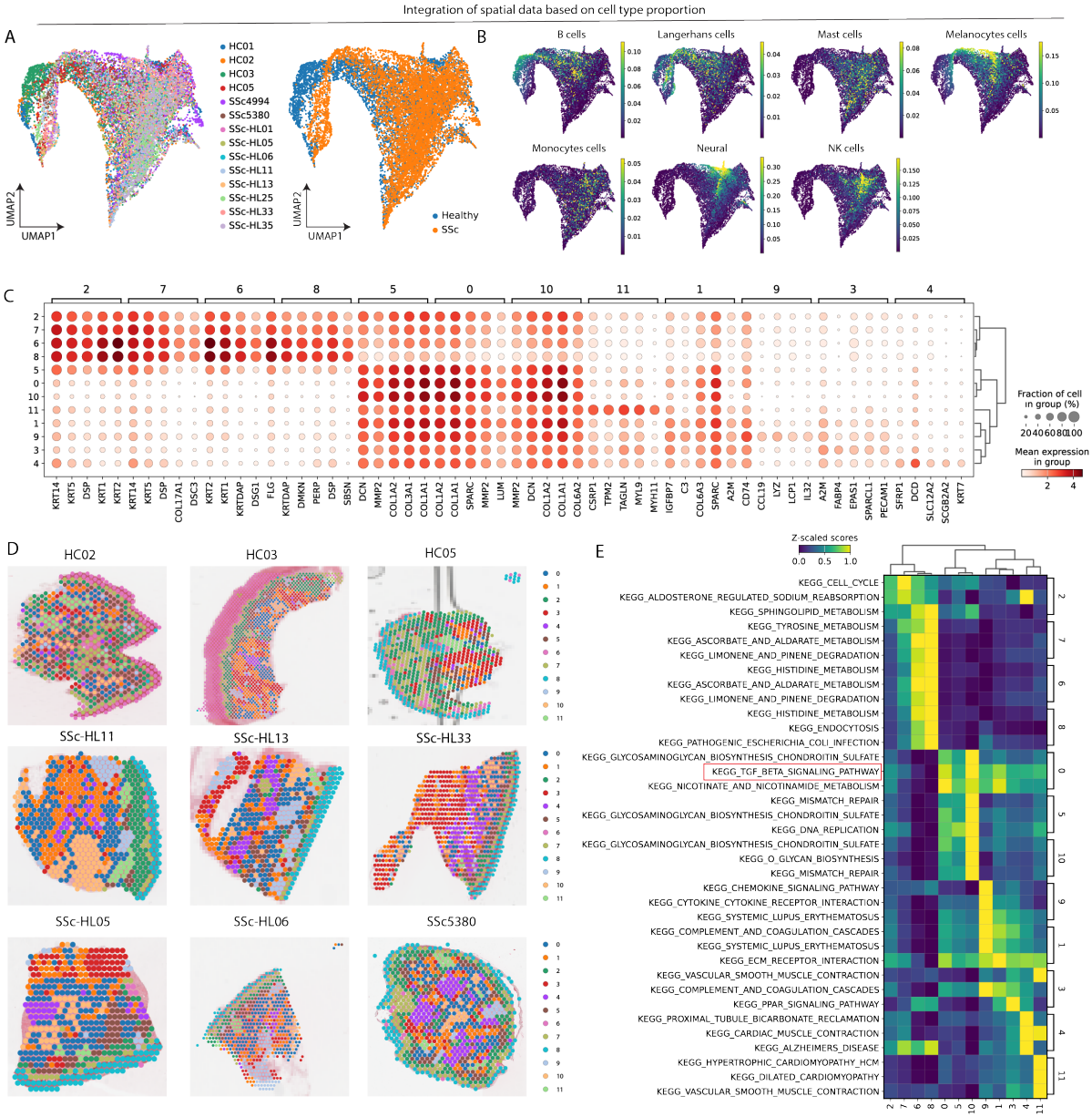

Fig. S3 Characterization of cell-type niches in human skin. (**A-B**), UMAP embedding of the integrated spatial data as colored by samples, conditions, and the fraction of each cell type. (**C**), Marker genes of each cell-type niche. (**D**), Visualization of cell-type niches in spatial space. (**E**), KEGG pathway enrichment analysis for each cell-type niche.

294 **Fig.S4**

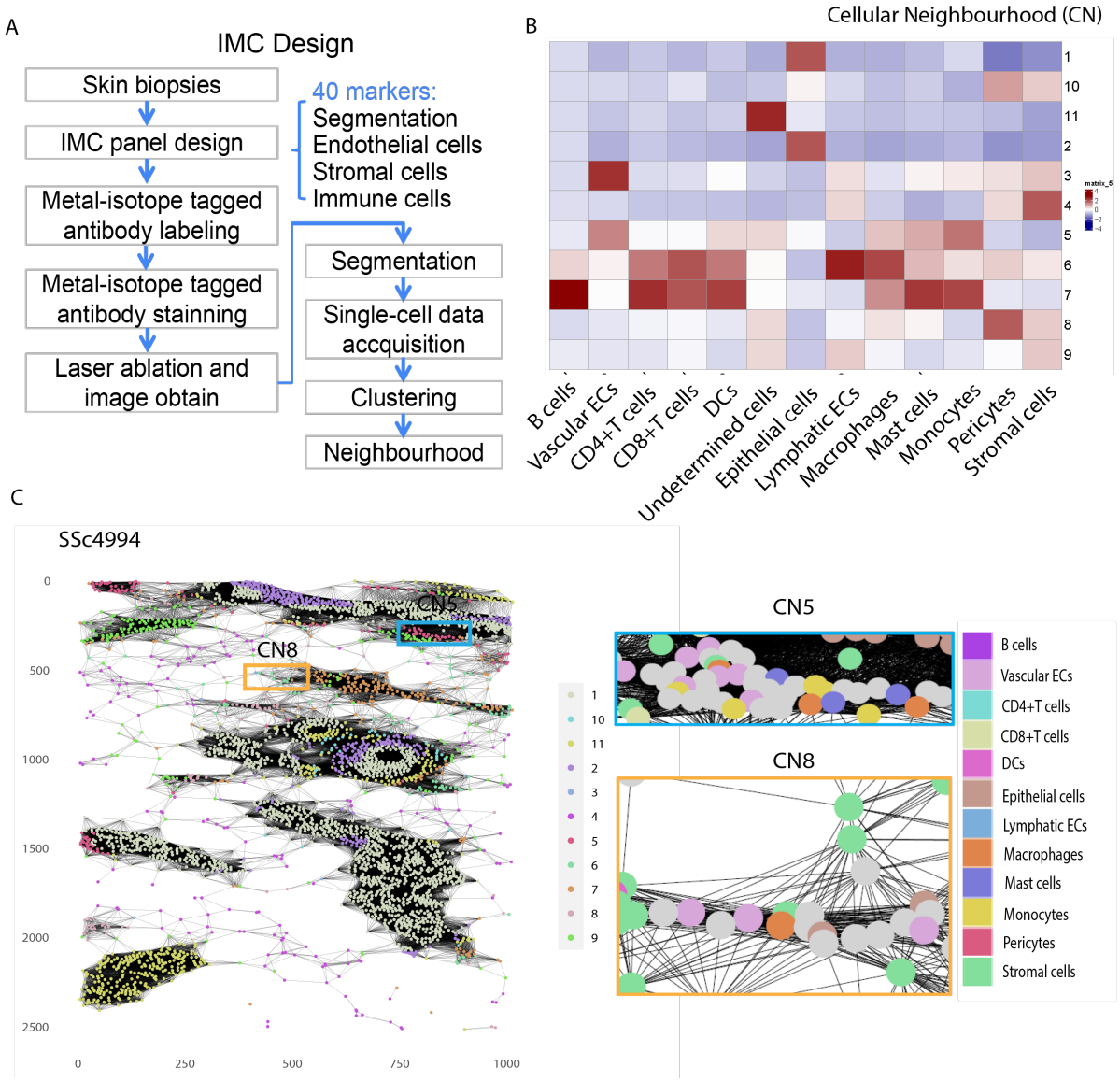

295

296 **Fig. S4 Validation of cellular neighborhood (CN) by imaging mass cytometry (IMC) in**
297 **healthy and SSc skin.** (**A**), Study design of IMC, as a validation spatial approach. We collected
298 skin biopsies from 19 SSc patients and 14 healthy controls as we previously described(*15*). (**B**),
299 Heatmap showing the enrichment of cell types in CNs. Each column represents a cell type, and
300 each row represents a CN. Colors refer to the proportions of each cell type across different CNs.
301 (**C**), Left: CN community detected using IMC. Colors refer to cellular clusters. Right: CN5 and
302 CN8 are highlighted and colored by cell types.

303

304

305

Fig.S5

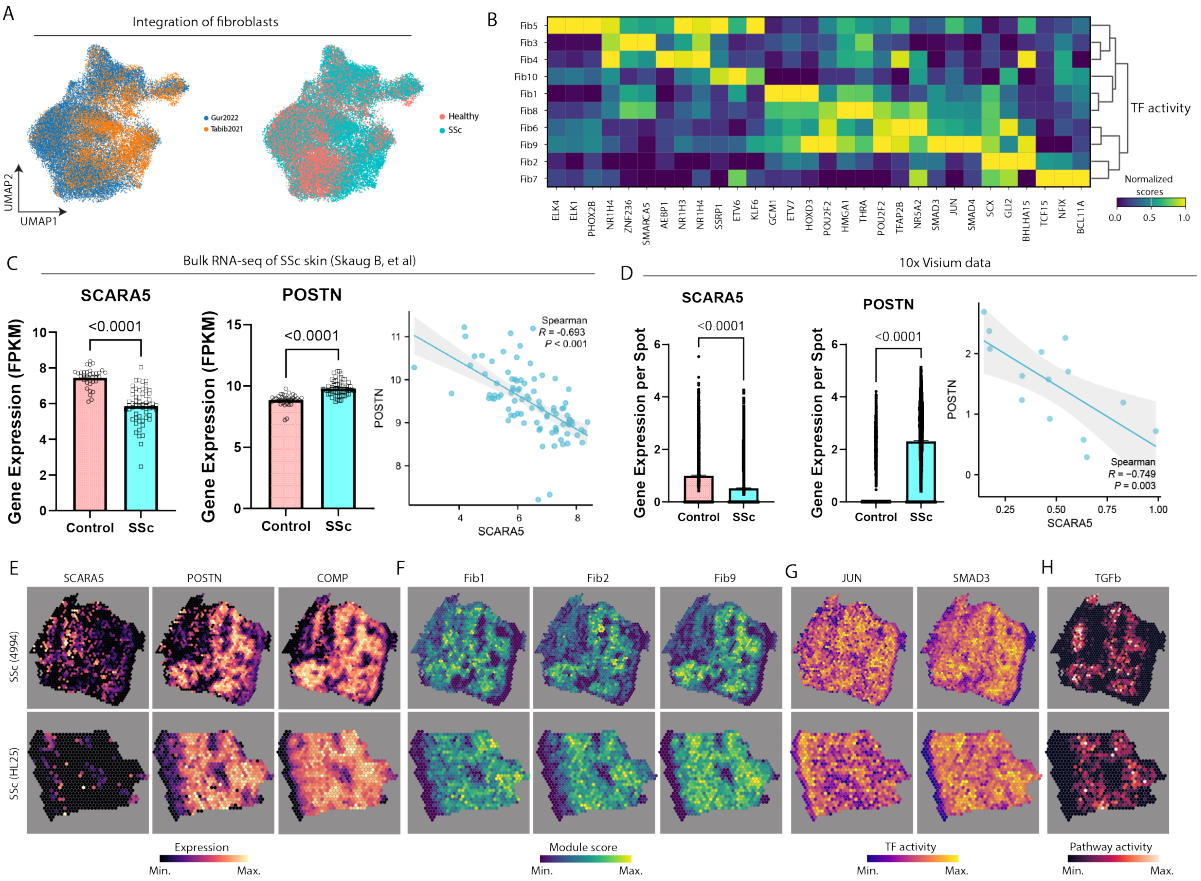

Fig. S5 Sub-clustering of fibroblasts. (**A**), UMAP embedding of the integrated scRNA-seq fibroblasts as colored by datasets and conditions. (**B**), Heatmap of top four marker transcription factors (TFs) for each sub-cluster-based TF activity score. (**C**), Left: barplot comparing the expression of *SCARA5* and *POSTN* between healthy and SSc conditions using bulk RNA-seq. Right: scatter plot showing the Spearman correlation between *SCARA5* and *POSTN* across patients. (**D**), Left: barplot comparing the expression of *SCARA5* and *POSTN* between healthy and SSc conditions using Visium data. Right: scatter plot showing the Spearman correlation between *SCARA5* and *POSTN* across Visium samples. (**E-H**), Visualization of marker genes (E), module scores (F), TF activity (G) and pathway activity (H) in spatial space.

Fig.S6

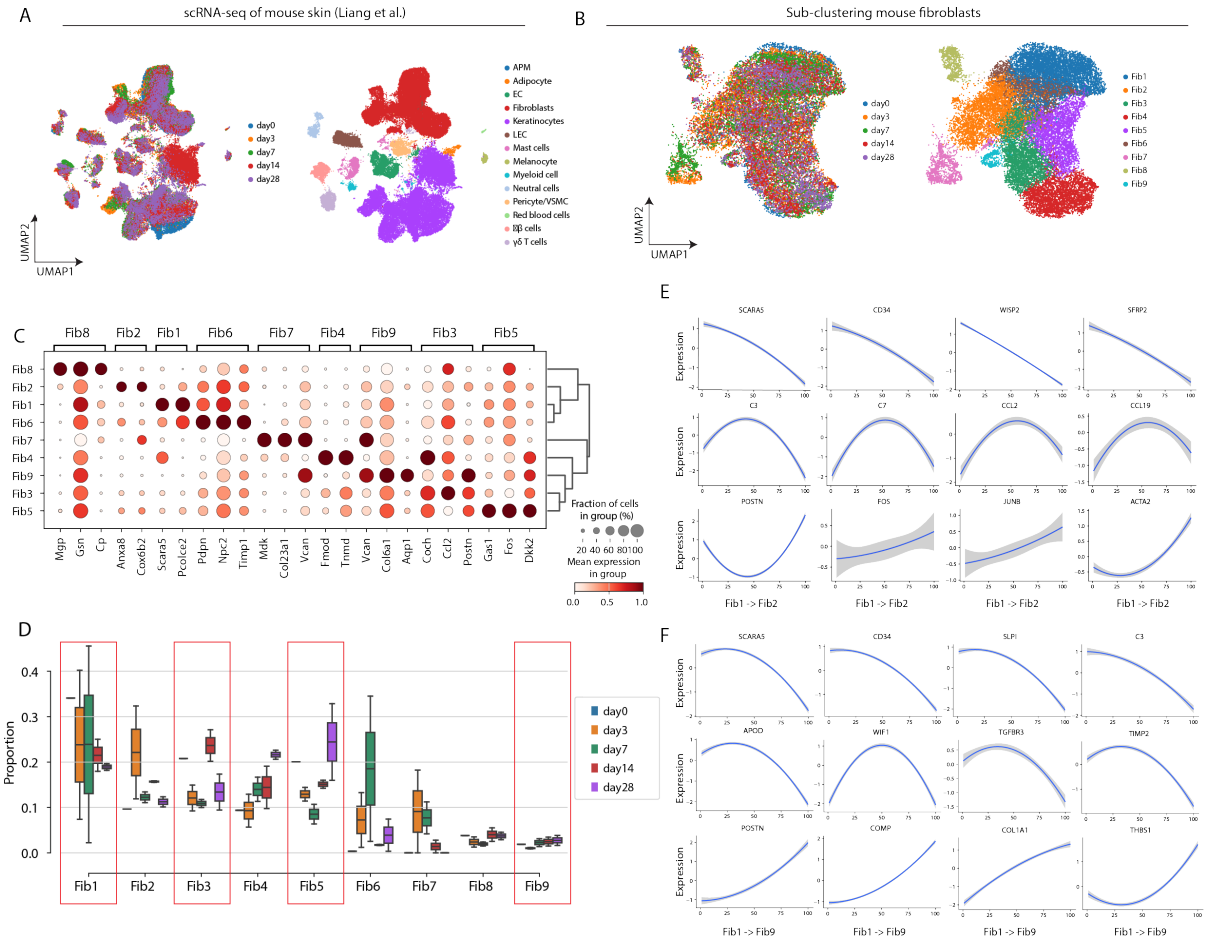

Fig. S6 Trajectory analysis of fibroblast differentiation. (**A**), UMAP of scRNA-seq data from mouse skin(*26*) colored by time points (left) after bleomycin (BLM) treatment and annotated cell types (right). (**B**), UMAP of fibroblasts colored by time points (left) and sub-clusters (right). (**C**), Dot plots of marker genes for each sub-cluster. The colors refer to the mean expression of the gene, and the size represents the fraction of cells that expressed the gene. (**D**), Box plot showing the fraction of each sub-cluster within different time points. (**E**), Line plot showing expression dynamics of selected genes along the differentiation trajectory from Fib1 to Fib2. (F), Line plot showing expression dynamics of selected genes along the differentiation trajectory from Fib1 to Fib9.

Fig.S7

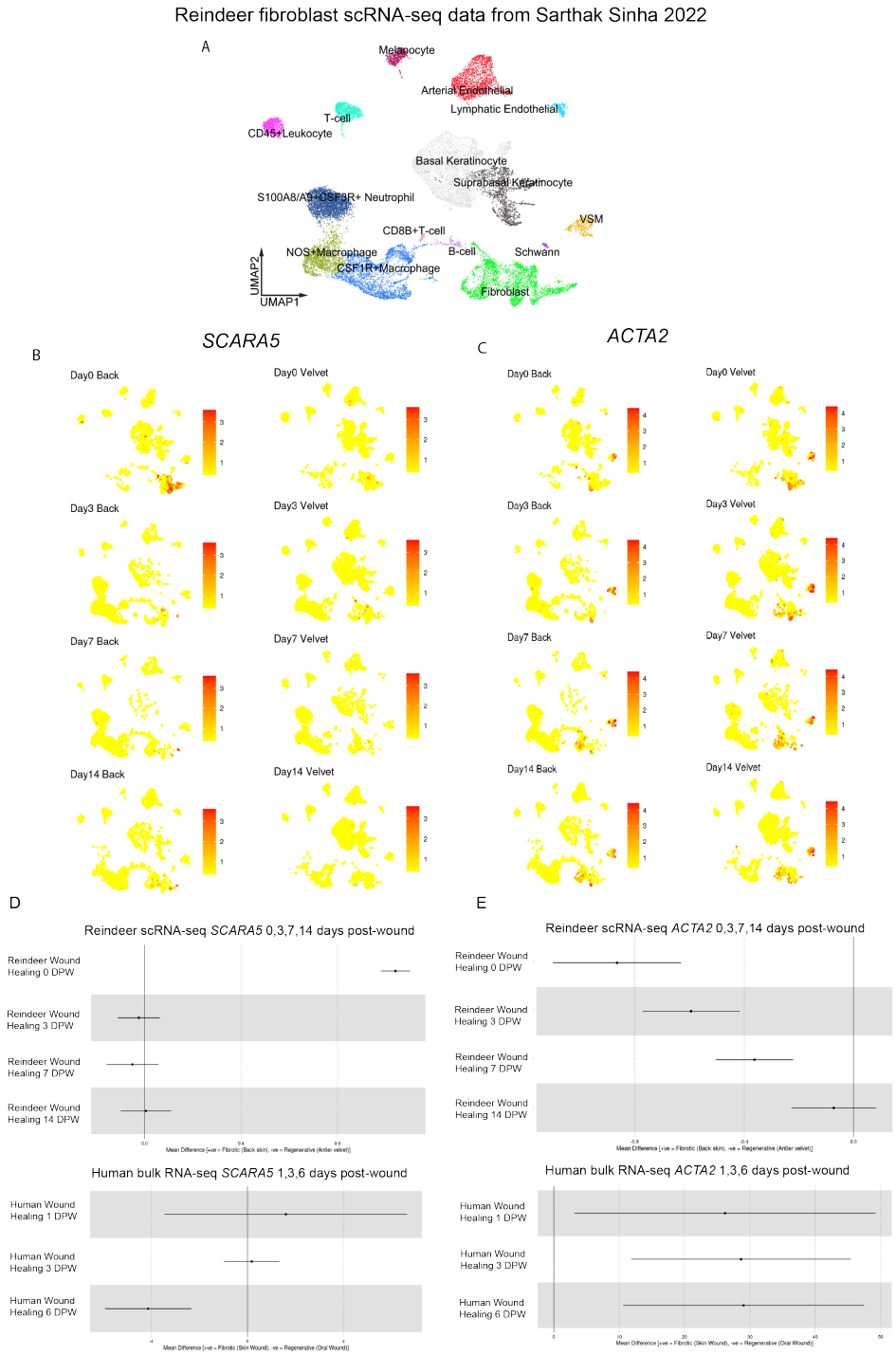

Fig. S7 Cross-Species Validation of Fibroblast Dynamics. Sarthak Sinha et al. utilized single-cell multi-omics to investigate full-thickness skin injuries in reindeer, revealing that their antler skin (velvet) regenerates, while their back skin forms fibrotic scars(*7*). (**A**), UMAP of scRNA-seq data from reindeer skin colored by cell type. (**B**, **C**), Visualization of *SCARA5* (b) and *ACTA2* (c) expression in UMAP, showing the gene expression on the back (left) and on the velvet (right). (**D**, **E**), Line plot showing expression dynamics of *SCARA5* and *ACTA2*

at the indicated days post wound in reindeer.

Fig.S8

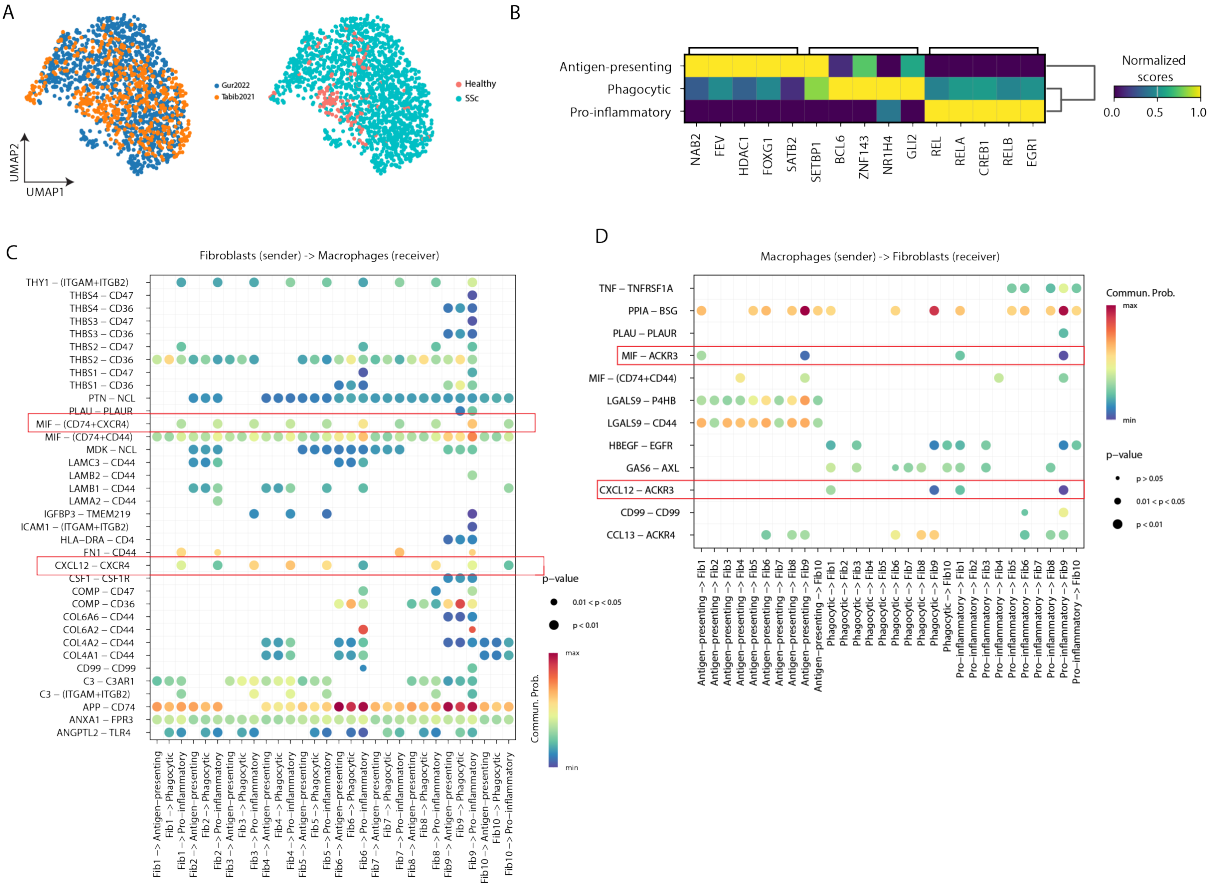

Fig. S8 Sub-clustering of macrophages. (**A**), UMAP showing scRNA-seq of macrophages colored different datasets (left) and conditions (right). (**B**), Heamap of top four marker TFs for each sub-cluster-based TF activity score. (**C**), Heatmap showing all significant L-R pairs from fibroblasts to macrophages. (**D**), Heatmap showing all significant L-R pairs from macrophages to fibroblasts.

367 **Table. S1 Clinical characterization of the patients with SSc**

368 **undergoing skin biopsy for spatial transcriptomic study**

Characteristics	N=10
Gender (female/male)	4/6 (40%/60%)
Median age at biopsy (range), years	56.0 (27-73)
Subsets (dcSSc/lcSSc)	10/0 (100%/0%)
Median disease duration from first non-RP (range), months	8 (4-48)
Disease duration (early/late) *	10/0 (100%/0%)
Median total mRSS (range) †	21 (8-41)
Progression of skin fibrosis with increases in total mRSS ‡	10/0 (100%/0%)
Active digital ulcer (s)	3 (30%)
Interstitial lung disease ‖	4 (40%)
Pulmonary arterial hypertension	2 (20%)
Estimated systolic pulmonary artery pressure (sPAP) >30 mm Hg#	3 (30%)
CRP (mg/dL)	9.30 (1.49-45.38)
Disease specific autoantibodies	
ATA positive	3 (30%)
ARA positive	4 (40%)
Anti-nRNP	1 (10%)
Anti-Ku	1 (10%)
Laboratory features	
Hemoglobin (g/L) (Median, IQR)	116.5, 100.0-136.0
Leukocytes (10^3/ul) (Median, IQR)	6.46, 4.11-14.99
Platelets (10^3/ul) (Median, IQR)	228, 120-363
CRP (mg/l) (Median, IQR)	4.60, 2.21-12.65

* as categorized by the duration from first non-RP symptoms (early ≤ 36 months;

late > 36 months); † as referred to the total mRSS assessed at 17 body sites; ‡ as defined by increase in total mRSS ≥ 25% from baseline to the follow-up visit within 52 weeks; || as detected by lung high-resolution CT; # as assessed by B-MODE Doppler echocardiography.

369

370 **Table. S2 Quality statistics for 10x Visium and Stereo-seq data**

sample	n_spot	condition	median_n_genes	median_n_UMIs	protocol
HC01	2035	Healthy	927	1170	Visium
HC02	663	Healthy	1861	2517	Visium
HC03	1805	Healthy	4096	8438	Visium
HC05	827	Healthy	2352	3341	Visium
SSc-HL01	453	SSc	3477	6437	Visium
SSc-HL05	508	SSc	2864	5895.5	Visium
SSc-HL06	612	SSc	3253.5	5587.5	Visium
SSc-HL11	695	SSc	1266	1850	Visium
SSc-HL13	605	SSc	1056	1495	Visium
SSc-HL25	751	SSc	1757	2935	Visium
SSc-HL33	737	SSc	2247	3629	Visium
SSc-HL35	877	SSc	3087	5945	Visium
SSc4994	1745	SSc	2238	3575	Visium
SSc5380	891	SSc	1482	1980	Visium
HC01	17089	Healthy	212	272	Stereo-seq
HL05	3437	SSc	330	440	Stereo-seq
HL25	10928	SSc	226	289	Stereo-seq
HL35	9112	SSc	184	234	Stereo-seq

371